The Application and Effects of Winglets on Wind Turbines

Bachelor Thesis in Mechanics and Maritime Sciences

Alexander Gustafsson
Felicia Häggström
Axel Johansson
Cesar Lanner
Joacim Suomi Forssblad

Department of Mechanics and Maritime Sciences
CHALMERS UNIVERSITY OF TECHNOLOGY
Gothenburg, Sweden 2024
www.chalmers.se

Bachelor Thesis 2024

The Application and Effects of Winglets on Wind Turbines

Alexander Gustafsson
Felicia Häggström
Axel Johansson
Cesar Lanner
Joacim Suomi Forssblad

CHALMERS

Department of Mechanics and Maritime Sciences
Division of Fluid Mechanics
Chalmers University of Technology
Gothenburg, Sweden 2024

The Application and Effects of Winglets on Wind Turbines

Alexander Gustafsson
Felicia Häggström
Axel Johansson
Cesar Lanner
Joacim Suomi Forssblad

Supervisor: Thisal Mandula Sugathapala, Mechanics and Maritime Sciences
Examiner: Niklas Andersson, Mechanics and Maritime Sciences

Bachelor thesis 2024
Department of Mechanics and Maritime Sciences
Chalmers University of Technology
SE-412 96 Gothenburg
Telephone +46 31 772 1000

Cover Image: Velocity magnitude on wind turbine, CFD simulation

Typeset in LaTeX
Gothenburg, Sweden 2024

Abstract

Ongoing research in the field of horizontal-axis wind turbines (HAWT) is dedicated to enhancing efficiency to maximize power generation. This bachelor's thesis provides an in-depth exploration of the impact of blade modifications, specifically the addition of winglets, on wind turbine performance. The study draws upon existing literature on winglets, utilizes Computational Aided Design (CAD), and use Computational Fluid Dynamics (CFD) simulations to investigate the effects comprehensively.

Three distinct winglets, each featuring different cant angles, were examined and compared. All winglet configurations were oriented towards the pressure side of the blade, with their height set to 1.5% of the blade radius. Furthermore, a wind turbine configuration without winglets served as a baseline for comparative analysis.

Results showed that regardless of winglet design, the overall power output decreased. The thrust force however experienced a higher decrease compared to the power output, resulting in an higher power to thrust ratio. Regarding the Turbulent Kinetic Energy (TKE), the winglets had no noticeable effect compared to the standard blades. Further, the pressure coefficient around the blades indicated that the addition of winglets resulted in a lower pressure area close to the hub, but remained rather similar at the tip of the blade. Results also showed that the addition of winglets increased the skin friction coefficient, implying a corresponding rise in drag force.

Keywords: Winglets, Wind turbine, Sustainability, CFD, Fluid Dynamics, Aerodynamics, power coefficient

Acknowledgements

Firstly, we would like to thank our supervisor Thisal Mandula Sugathapala, PhD Student in the Mechanics and Maritime Sciences Department, for his help and support throughout this project.

Secondly, we would like to thank our examiner Niklas Andersson, Professor in the Mechanics and Maritime Sciences department, for helping us with this thesis.

A. Gustafsson, F. Häggström, A. Johansson, C. Lanner, J. Suomi Forssblad
Gothenburg, May, 2024

Acronyms

Below is the list of acronyms that has been used throughout the entire dissertation listed in alphabetical order:

CAD	Computational Aided Design
CFD	Computational Fluid Dynamics
FVM	Finite Volume Method
HAWT	Horizontal Axis Wind Turbine
NAISS	National Academic Infrastructure of Supercomputing in Sweden
NASA	National Aeronautics and Space Administration
RST	Reynolds Stress Transport Models
TKE	Turbulent Kinetic Energy
URANS	Unstable Reynolds Average Navier Stokes
VRP	Virtual Rotating Part
VWT	Virtual Wind Tunnel

Nomenclature

Below is the list of nomenclature that has been used throughout the entire dissertation listed in alphabetical order:

Indices

i,j	Tensor notations

Fluid dynamic variables

a	Acceleration $[ms^{-2}]$
a_i	Induction factor [-]
C_f	Skin friction coefficient [-]
C_P	Power coefficient [-]
C_{pr}	Pressure coefficient [-]
cs	Control surface [-]
F	Force $[N]$
F_D	Drag force $[N]$
F_L	Lift force $[N]$
f_i	External forces $[N]$
h	Height $[m]$
k	Turbulence Kinetic Energy $[m^2s^{-2}]$
L	Characteristic length $[m]$
m	Mass $[kg]$
$\dot{m}$	Mass flow $[kgs^{-1}]$
P_t	Extracted power $[W]$
p	Static pressure $[Pa]$
p_∞	Static pressure in the freestream $[Pa]$

R	Radius of swept area $[m]$
Re	Reynolds number
S_{ij}	Strain-rate tensor $[s^{-1}]$
T_N	Thrust force $[N]$
T_Q	Torque force $[N]$
t	Time $[s]$
u	Flow velocity in x-direction $[ms^{-1}]$
V	Fluid velocity $[ms^{-1}]$
V_∞	Freestream velocity $[ms^{-1}]$
V_d	Disc velocity $[ms^{-1}]$
V_w	Velocity at the wake $[ms^{-1}]$
v	Flow velocity in y-direction $[ms^{-1}]$
w	Flow velocity in z-direction $[ms^{-1}]$
δ_{ij}	Kroneckers delta [-]
λ	Tip speed ratio [-]
μ	Dynamic viscosity $[kgm^{-1}s^{-1}]$
ν	Kinematic viscosity $[m^2s^{-1}]$
ρ	Density $[kgm^{-3}]$
τ_w	Wall shear stress $[Pa]$
ω	Angular velocity $[radt^{-1}]$

Fluid dynamic constants

g	Gravitational acceleration $[ms^{-2}]$
π	Archimedes constant [-]

Contents

List of Figures

List of Tables

1
Introduction

1.1 Background

As the demand for renewable energy continues to rise, resources are being allocated to the development of wind turbines [1]. It is therefore important that these turbines achieve optimal efficiency. Despite the rapid advancements in efficiency and scale witnessed by wind turbines in the last decades, there are still technological improvements yet to be discovered [2].

In recent years, wind turbines have undergone significant growth in both height and size, aimed at maximizing energy generation [2]. However, efficiency is not solely determined by these factors. Wind turbines rotate due to aerodynamic lift generated by pressure differences on the blades. Additionally, drag, a retarding force acting on the turbine blades, decreases the lift force and thus reduces efficiency [3]. Optimizing the geometry and shape of the blades can improve the ratio between lift and drag forces, thereby enhancing power output. When exploring potential improvements, insights from other aerodynamic industries, such as aviation, could offer valuable information and knowledge. Their extensive experience in optimizing aerodynamic surfaces can be taken advantage of when investigating further improvements in wind turbine design.

An innovation developed by the aviation industry, the *winglet device*, has become a common feature on commercial airliners. These devices enhance wing efficiency by reducing vortices generated at the wingtip. These vortices contribute to an induced drag force on the wing, which in turn reduces efficiency [4]. In that way, the winglet design increases lift generation, resulting in a more efficient wing. This design principle holds promise for application to wind turbines, with several studies suggesting that winglets can enhance aerodynamic efficiency [5]. However, further research is still needed to fully understand the effects and any potential benefits. This report aims to contribute to this ongoing investigation by exploring the impact of winglet devices on wind turbine aerodynamic efficiency.

1.2 Purpose

The aim of this study is to investigate the application of winglet devices on wind turbine blades and determine their impact on aerodynamic performance. The study will compare winglets with various cant angles and analyze their potential contribution to increased efficiency. The goal of this project is to broaden the knowledge regarding winglets on wind turbines.

1.3 Delimitation

This project has chosen to evaluate winglets on a horizontal axis wind turbine (HAWT). Therefore, other designs of wind turbines will not be examined.

The wind turbine designs will only be simulated and tested virtually using CFD, meaning that real prototypes will not be manufactured and tested. The performance of a real model compared to a virtual one will therefore not be validated and analyzed. Further, the models used will be a scaled down version of an existing CAD model in order to reduce the computational cost when simulating.

Another delimitation of this project is the number of parameters changed. A winglet can be designed in several ways, however, this project will only investigate the performance of different cant angles pointed towards the pressure side of the blade. Therefore, the other angles will be set to zero and the height will remain constant. This is mainly due to the restricted amount of core hours the project has access to and the time frame of the project. The rotor-radius of the wind turbine as well as all other parameters regarding winglet design and geometry will therefore remain constant for all the different designs.

When simulating, the flow around the wind turbines is considered to be incompressible. If air moves slower than 30% of the speed of sound, it can be considered incompressible [6]. The velocities used in this study are far below these numbers, which validates the assumption.

In addition to the delimitation regarding design and simulation, the study will not investigate how winglets affect the surrounding environment. Sound, vibration, and interference with animals such as birds will not be evaluated, since the intent of this study solely is to investigate performance and aerodynamic efficiency. Further, economic aspects will also be disregarded, and any potential additional manufacturing costs of wind turbines with winglets will not be calculated.

2
Theory

In this chapter, information regarding the fundamental physics and aerodynamics behind wind turbines are described. The usage of the theory in this report will also be explained, and how they are implemented when analyzing different models of wind turbines. Additionally, details regarding Computational Fluid Dynamics (CFD) simulation and setup will be explained.

2.1 Fundamental fluid dynamics theory

This section explains the fundamental physics and aerodynamics behind wind turbines and how they operate. Further, fluid dynamics theory used in CFD simulations are also presented. All variables can be found in the Nomenclature.

2.1.1 Bernoulli's equation

For an incompressible, steady, and frictionless flow along a streamline, Bernoulli's equation can be derived from the conservation of energy as:

$$p + \frac{1}{2}\rho V^2 + \rho g h = constant \tag{2.1}$$

where h is the elevation above a set reference plane, with the positive direction opposite to the gravitational acceleration. This law states that as pressure decreases, the velocity must increase [6]. This relation is helpful when understanding how wind turbines generate lift, which is explained more in-depth in section 2.3.1.

2.1.2 Conservation of mass and linear momentum

In mechanics, a system is defined as a fixed quantity of mass [6]. That is, the mass does not change. If the mass is denoted by m, it can be expressed as:

$$\frac{dm}{dt} = 0 \tag{2.2}$$

This relation is called the *conservation of mass*. Further, if the mass is being exposed to a force, it will begin to accelerate according to Newton's second law [6]. In fluid dynamics, Newton's second law is called *the linear momentum relation* and can be written as:

$$\mathbf{F} = m\mathbf{a} = m\frac{dV}{dt} = \frac{d}{dt}(m\mathbf{V}) \tag{2.3}$$

where $\mathbf{a}$ is the acceleration vector and $\mathbf{V}$ is the velocity vector [6]. The property $(m\mathbf{V})$ is called the linear momentum. For a fixed control volume, cv, the sum of all forces acting on the system can be expressed as:

$$\sum \mathbf{F} = \frac{d}{dt}\left(\int_{cv} \rho \mathbf{V} d\mathcal{V}\right) + \int_{cs} \rho \mathbf{V}\left(\mathbf{V} \cdot \mathbf{n}\right) dA \tag{2.4}$$

The surface integral in the equation is called the *momentum flux term* [6]. If the cross-section is one-dimensional and the system is in steady-state, the equation can be rewritten as:

$$\sum \mathbf{F} = \sum(\dot{m}_i \mathbf{V}_i)_{out} - \sum(\dot{m}_i \mathbf{V}_i)_{in} \tag{2.5}$$

where $\dot{m}$ is defined as the *mass flow*. This relation is called *the conservation of momentum*. A deeper explanation regarding how these equations are implemented on wind turbines can be found in section 2.3.3.

2.1.3 The continuity equation

The conservation of mass within a fixed control volume can be described as:

$$\frac{\partial \rho}{\partial t} + \nabla \cdot (\rho \mathbf{V}) = 0 \tag{2.6}$$

where $\mathbf{V}$ is the flow velocity. If the flow is incompressible, the density can be seen as constant since it does not change with time and space. Thus the equation becomes:

$$\nabla \cdot (\rho \mathbf{V}) = 0 \quad \Longrightarrow \quad \nabla \cdot (\mathbf{V}) = 0 \tag{2.7}$$

This equation states that the mass flow through a closed channel will be conserved [6].

2.1.4 Navier-Stokes equations

For an incompressible and Newtonian fluid, a fluid can be described with the help of the Navier-Stokes equation:

$$\frac{du}{dx} + \frac{dv}{dy} + \frac{dw}{dz} = 0 \tag{2.8}$$

$$\rho g_x - \frac{\partial p}{\partial x} + \mu \left(\frac{\partial^2 u}{\partial x^2} + \frac{\partial^2 u}{\partial y^2} + \frac{\partial^2 u}{\partial z^2} \right) = \rho \left(\frac{du}{dt} + u\frac{du}{dx} + v\frac{du}{dy} + w\frac{du}{dz} \right) \tag{2.9}$$

$$\rho g_y - \frac{\partial p}{\partial y} + \mu \left(\frac{\partial^2 v}{\partial x^2} + \frac{\partial^2 v}{\partial y^2} + \frac{\partial^2 v}{\partial z^2} \right) = \rho \left(\frac{dv}{dt} + u\frac{dv}{dx} + v\frac{dv}{dy} + w\frac{dv}{dz} \right) \tag{2.10}$$

$$\rho g_z - \frac{\partial p}{\partial z} + \mu \left(\frac{\partial^2 w}{\partial x^2} + \frac{\partial^2 w}{\partial y^2} + \frac{\partial^2 w}{\partial z^2} \right) = \rho \left(\frac{dw}{dt} + u\frac{dw}{dx} + v\frac{dw}{dy} + w\frac{dw}{dz} \right) \tag{2.11}$$

where u is the velocity in x-direction, v is the velocity in y-direction and w is the velocity in z-direction. This is a part of the governing equations that are used in CFD when solving the problem geometry and will be explained further in section 2.5 [7].

2.1.5 Unsteady Reynolds-Averaged Navier-Stokes

Unsteady Reynolds-Averaged Navier-Stokes (URANS) refers to a reduced form of the Navier-Stokes equations expressed in section 2.1.4 using Reynolds decomposition. Reynolds decomposition is used to derive the URANS equations, which is applied by time-averaging the Navier-Stokes equations. The flow velocity can be separated into two parts, one time-independent mean flow velocity and one time-varying fluctuation [6]:

$$\phi = \overline{\phi} + \phi' \tag{2.12}$$

where ϕ is an arbitrary constant.

The decomposition can be used to derive the nonlinear expression of the flow:

$$\rho \frac{\partial \bar{u}_i}{\partial t} + \rho \bar{u}_j \frac{\partial \bar{u}_i}{\partial x_j} = \rho \bar{f}_i + \frac{\partial}{\partial x_j} \left[-\bar{p}_j \delta_{ij} + 2\mu \bar{S}_{ij} - \rho \overline{u_i' u_j'} \right] \tag{2.13}$$

where $\bar{f}_i$ is time average of a vector describing external forces and $\bar{S}_{ij}$ is the mean rate of strain tensor, expressed as $\bar{S}_{ij} = \frac{1}{2}\left(\frac{\partial \bar{u}_i}{\partial x_j} + \frac{\partial \bar{u}_j}{\partial x_i}\right)$.

These equations are used in the CFD turbulence models that will be used in this study, and their main purpose is to govern the transport of the mean flow quantities in the simulations [8][p. 4434].

URANS is an appropriate method for thermal transient simulations problems, where large time periods are of more importance than local flow structure [8]. Thermal transient simulations describe the system response of fixed and time-varying boundary conditions [9].

2.1.6 Turbulence Kinetic Energy

The Turbulence Kinetic Energy (TKE) is the kinetic energy per unit mass of the turbulent fluctuations in a turbulent flow [10]. It measures the intensity of turbulence in a flow and is defined as:

$$k = \frac{1}{2}(\bar{u}'^2 + \bar{v}'^2 + \bar{w}'^2) \tag{2.14}$$

k is the TKE. $\bar{u}'$, $\bar{v}'$ and $\bar{w}'$ are the time-varying velocity components.

2.2 Dimensionless parameters

Dimensionless parameters are scalar quantities commonly used in fluid dynamics [6]. If two systems have equal dimensionless parameters and equal but scaled geometries, the dimensionless parameters will derive the boundary conditions for the scaled geometry [6]. This makes them a useful tool when modeling, allowing for comparison between different systems by comparing their dimensionless parameters. Down below, the parameters of relevance in this study are presented.

2.2.1 Reynolds number

The Reynolds number is a useful parameter within the field of fluid dynamics and is used to determine the viscous behavior of a flow. Lower values indicate laminar flow meanwhile larger values indicate turbulent flow [6]. Very low values indicate a so-called viscous creeping flow, where the viscous forces dominate and the internal forces are negligible. Mathematically, the Reynolds number gives the ratio between inertial forces and viscous forces in a fluid due to relative movement caused by fluid velocities [6]. The equation is written as follows:

$$Re = \frac{\rho V L}{\mu} = \frac{V L}{\nu} \tag{2.15}$$

L is the characteristic length and μ is the dynamic viscosity of the flow [6]. The Reynolds number could also be expressed with the kinematic viscosity ν, which is the dynamic viscosity divided by the density of the fluid.

In wind tunnel testing and CFD simulations, the Reynolds number is especially important and helpful. Assuming geometric similarity, matching this parameter enables the use of scaled models and ensures accurate simulations when analyzing the flow patterns of those models and relating them to the real prototype. In other words, it can be used to achieve dynamic similarity [11].

2.2.2 Power coefficient

The power coefficient, C_p, is a dimensionless variable that expresses the ratio between extracted power relative to the energy available in the wind. It is used when evalu-

ating the efficiency of the wind turbine and is defined as:

$$C_p = \frac{P_t}{\frac{1}{2}\rho\pi R^2 V_\infty^3} \tag{2.16}$$

P_t is the power extracted by the wind turbine, πR^2 is the swept area and V_∞ is the freestream velocity [6]. The nominator expresses the mass flow through the propeller times the kinetic energy of the wind [6]. This parameter will be used in this report when comparing the different models, to investigate potential differences regarding their power efficiency. A deeper explanation for how this parameter is implemented in this study can be found in section 2.3.4.

2.2.3 Pressure coefficient

The pressure coefficient, C_{pr}, is a dimensionless parameter that describes the relative pressure through a flow field and is defined as:

$$C_{pr} = \frac{p - p_\infty}{\frac{1}{2}\rho V^2} \tag{2.17}$$

p is the static pressure at the point of interest and p_∞ is the static pressure in the freestream [6].

2.2.4 Skin friction coefficient

The skin friction coefficient, C_f, is a dimensionless parameter that relates the wall shear stress to the dynamic pressure [6]. It is defined as:

$$C_f = \frac{\tau_w}{\frac{1}{2}\rho V^2} \tag{2.18}$$

where τ_w is the wall shear stress.

2.3 Application of fluid dynamics on horizontal-axis wind turbines

Wind turbines have been used for centuries as a source of mechanical power. Today, the HAWT is the most common type [12]. It can be single-bladed, double-bladed, or three-bladed. In this study, the three-bladed HAWT will be used and studied.

2.3.1 Aerodynamic forces

Wind turbines rotate due to aerodynamic lift created by pressure differences between the front and rear sides of the blades [12]. When the incoming air encounters the blades, the wind turbine starts to rotate. However, due to the blades' own movement, the direction of the incoming wind from the blades' perspective changes. Further,

when the air meets the blades, fluid velocity increases on one side and decreases on the other. Following Bernoulli's principle in Equation 2.1, the pressure must decrease where the velocity is higher and increase where it is lower [6]. Seeking equilibrium, air on the higher-pressure side (pressure side) moves toward the lower-pressure side (suction side), creating a lift force (F_L) [12]. Lift acts perpendicular to the incoming airflow. On wind turbines, the pressure side forms on the upwind side of the blade, while the suction side forms on the downwind side.

In addition to the perpendicular lift force, the blade is affected by a force parallel to the flow called drag force (F_D). This force can be explained as the resistance force of the fluid [3]. The blade experiences both of these forces simultaneously and is used to describe the characteristics of the blade profile [13]. These two components are then together transformed into a pair of other forces called thrust force (T_N) and torque force (T_Q) [13] (see Figure 2.1). These transformed forces are commonly used in wind turbine aerodynamics and will be implemented when calculating the power of the wind turbine.

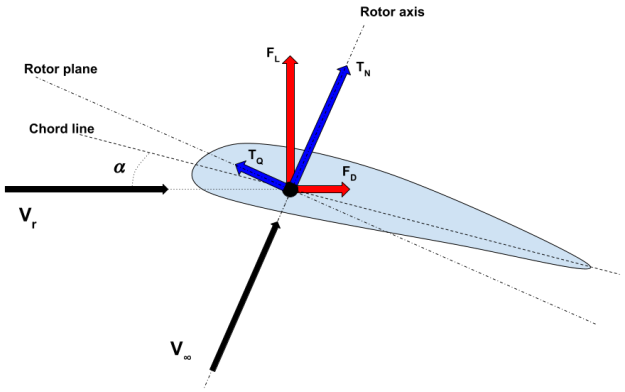

Figure 2.1: Aerodynamic forces

The attack angle, denoted as α, represents the angle between the chord line and the incoming wind direction [3]. V_∞ is the incoming wind and V_r is the wind from the rotating blades' perspective. The torque force contributes to the driving torque around the turbine's shaft, which, in conjunction with the angular velocity, determines the output power of the turbine (see Section 2.3.4) [14]. Conversely, the thrust force does not directly drive the turbine but imposes stress on the rotor blades, resulting in a thrust force exerted on the nacelle and tower [13].

2.3.2 Induced drag

Similar to aircraft wings, HAWT-blades are susceptible to induced drag [4]. As air on the pressure side of the blade seeks equilibrium with the suction side due to pressure differences, vortex flow is generated at the blade tip. This alters the airflow behind

the trailing edge, causing it to deflect downwards. This phenomenon is known as downwash, which increases induced drag [4]. This increased drag component negatively impacts turbine efficiency and impairs the ability to extract energy from the wind.

2.3.3 Actuator Disc Theory and Betz limit

Wind turbines generate electricity by extracting energy from the wind [15]. To get an understanding of how energy is extracted, the *actuator disc model*, illustrated in Figure 2.3.3, is used.

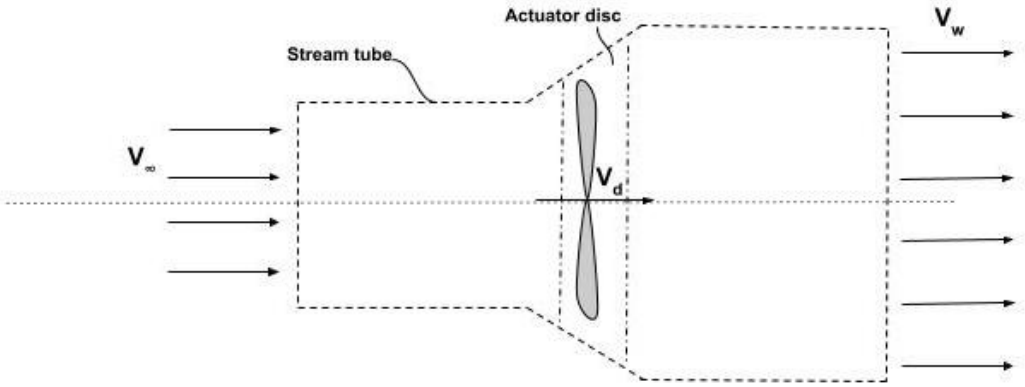

Figure 2.2: Actuator disc model

In the actuator disc model, the wind is represented by a streamtube, while the rotor is represented by an actuator disc. According to the continuity equation, the mass flow of the wind is conserved through both the streamtube and the disc (see Section 2.6) [15]. As the rotor extracts energy from the wind, the velocity decreases, resulting in an expansion of the wake to uphold the conservation of mass and momentum [6]. Assuming ideal conditions and one-dimensional flow, the power coefficient, as explained in Section 2.2.2, can be expressed using momentum theory as:

$$C_p = \frac{P_t}{\frac{1}{2}\rho\pi R^2 V_\infty^3} = 4a_i(1-a_i)^2 \tag{2.19}$$

where a_i is called the *induction factor* which can be written as:

$$a_i = \frac{V_\infty - V_d}{V_\infty} \tag{2.20}$$

The velocity of the incoming wind is denoted as V_∞, while V_d represents the velocity at the disc [16]. The maximum value of the power coefficient (C_p) is achieved by differentiating with respect to the induction factor (a_i) and setting it to zero, yielding an induction factor of $a_i = 1/3$. Consequently, the maximum value of C_p is $16/27 \approx 0.59$, known as the Betz limit [15] [16].

The Betz limit states that the maximum theoretical efficiency of a wind turbine is 59%. If all the energy available in the wind were fully extracted by the turbine, the wind velocity would drop to zero immediately after the actuator disc. This would block new wind from entering, preventing movement both in front of and behind the turbine for energy extraction to occur [16]. Present-day wind turbines achieve an efficiency of approximately 50%, indicating that there is still room for technical improvement [17].

2.3.4 Power coefficient for wind turbines

The efficiency of a wind turbine is dependent upon the speed of the incoming wind, as the total energy available is directly proportional to it. Consequently, the values of C_p vary for different wind velocities [18]. To relate the power coefficient's value to the wind speed, the *tip speed ratio* is used. The tip speed ratio is defined as the ratio of blade tip velocity to wind velocity [3]. Mathematically, the tip speed ratio can be expressed as:

$$\lambda = \frac{\omega R}{V_\infty} \tag{2.21}$$

where ω is the angular velocity, R is the rotor radius, and V_∞ is the velocity of the incoming wind [19].

The power extracted from the wind turbine (P_t) is calculated by multiplying the angular velocity and torque force (T_Q) of the wind turbine [14]. By replacing these parameters in equation 2.16, the equation becomes:

$$C_p = \frac{\omega T_Q}{\frac{1}{2}\rho\pi R^2 V_\infty^3} \tag{2.22}$$

This relation will be used when comparing the different power outputs of the wind turbine models.

2.4 Winglets

Winglets, as stated, is a device that today is commonly used in the aviation industry. Their purpose is to reduce the induced drag, and research has shown that adding winglets on wind turbines may improve their efficiency as well [14][20]. Even though winglets add excessive profile drag, numerical and experimental studies have shown

that if designed correctly, they can have a positive effect on the wind turbine performance [5].

2.4.1 Vortex reduction

As explained in section 2.1, when the incoming wind encounters the blade the air tries to move from the high-pressure to the low-pressure side. Consequently, this creates vortices behind the tip which in turn generates downwash. However, when adding winglets, these devices block the air trying to get from one side to the other, leaving just a small vortex at the tip of the winglet (see Figure 2.3).

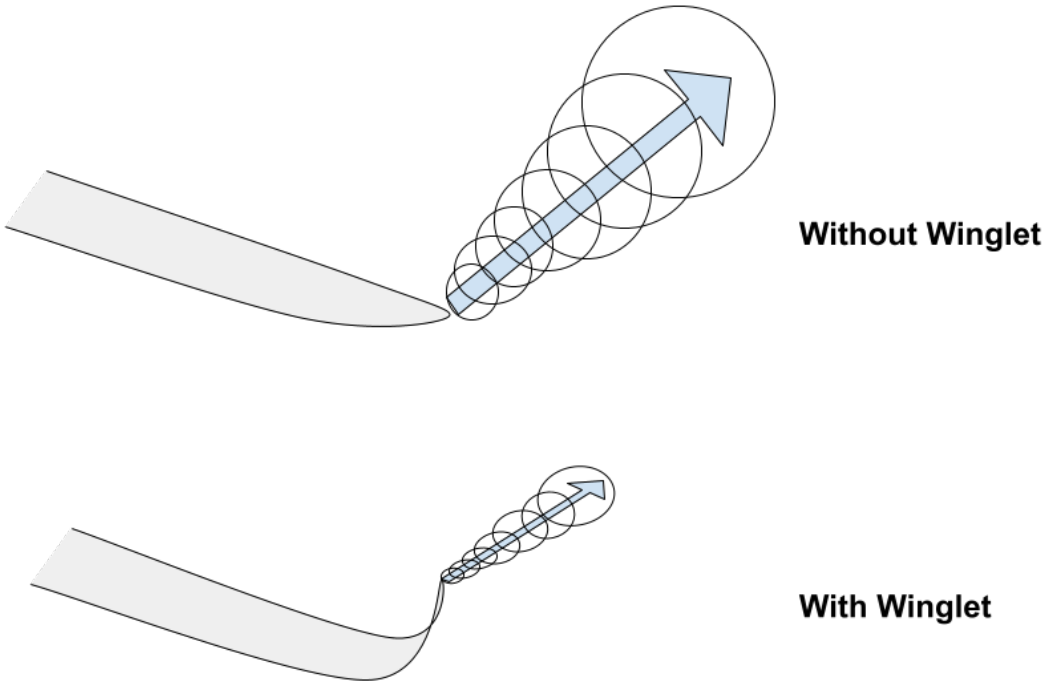

Figure 2.3: Vortices created with and without winglet

By reducing the downwash effect, the drag force component decreases, and the lift force increases. This means that a bigger proportion of the total force can be used to rotate the blades, resulting in more harvested energy from the turbine.

2.4.2 Winglet design

Winglets can be designed differently depending on usage and desired requirements, however, the intended effect of all designs is to reduce the induced drag. The main parameters for designing a winglet are height, cant angle, sweep angle, toe angle, and twist angle (see Figure 2.4).

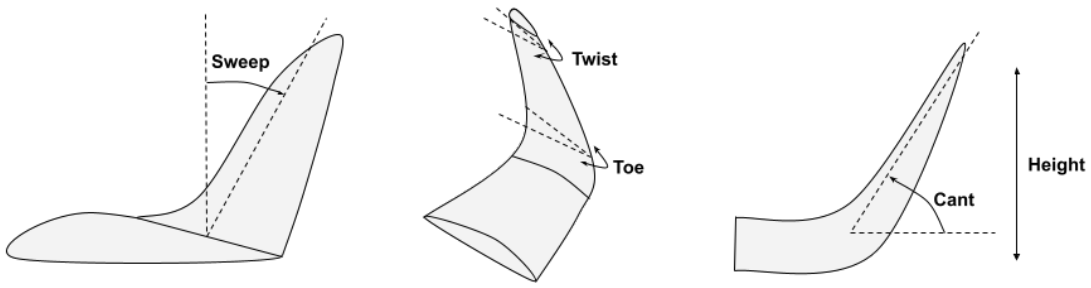

Figure 2.4: Winglet-design parameters

The sweep angle describes the angle between the span of the winglet and a line perpendicular to the centerline of the wing. The twist angle describes how much the winglet is twisted, and the toe angle defines the orientation of the winglet for the longitudinal vertical blade. The cant angle is defined as the angle at which the winglet is tilted from a theoretical flat wing extension [21].

2.5 Fundamentals of CFD

The governing Navier-Stokes equations are difficult to solve if they are not simplified due to the complexity of the equations [7]. To evaluate and analyze how an attached winglet will affect the airflow and efficiency of a wind turbine, computational fluid dynamics (CFD) is of great use [22]. CFD is a simulation tool that solves the Navier-Stokes equations with numerical approximations and returns field values such as velocities and pressures amongst other parameters of interest [22]. When using CFD, the procedure can be divided into three main steps; *pre-processing, simulation*, and *post-processing* [7].

2.5.1 Pre-processing

The pre-processing part of CFD contains CAD cleaning, generation of the grid and mesh, defining the physics models, defining the flow parameters, and setting up the initial boundary conditions [7][23]. Before running the simulation it is crucial to validate the setup and check for flaws, to get a legitimate result [7].

2.5.1.1 CAD cleaning

When working with CFD, the geometry model must be free of errors [24]. That is, the model should be a closed solid without any missing faces or gaps in the geometry [7]. Sharp edges and nodes can also be a problem since they can cause intersecting and overlapping faces [7]. After preparation, the model should be free of any of these defects [24], and the geometry should be a clean and continuous solid [7].

When the model is validated, the domains and regions need to be defined. The domain is a volumetric region that surrounds the problem geometry [25]. This is where the governing equations are solved.

2.5.1.2 Meshing

When the domains have been defined, they need to be meshed. A mesh is a network formed by cells and nodes [26]. The mesh can be of different shapes and sizes and each of the cells solves the partial differential equations individually. The individual solutions are then combined with the whole network to form one solution for the entire mesh. Further, at the boundary layer of the domain, the mesh can be made finer, this region is called the prism layer [26]. This can be implemented in order to get a boundary layer of better quality.

At the prism layer, in addition to the selection of shape and size of the cells, several input parameters need to be defined and calculated in order to solve the partial differential equations [26]. In this study, the following equations are used [27]:

$$\frac{Y^+}{FLT} = \frac{0.487}{\nu Ln(0.06Re_C)}V_r \tag{2.23}$$

$$V_r = \sqrt{V_\infty^2(R\omega)^2} \tag{2.24}$$

Y^+ is the dimensionless wall distance, FLT is the First Layer cell Thickness, ν is the kinematic viscosity, Re_C is the Reynolds Number based on chord length and V_r is the relative wind speed for the blade of the wind turbine.

$$\frac{\delta}{C} = \frac{0.16}{Re_c^{\frac{1}{7}}} \tag{2.25}$$

$$\delta = \frac{FLT(1-r^m)}{1-r} \tag{2.26}$$

δ is the boundary layer thickness, C is the chord length, R is the radius, ω is the angular velocity, r is the stretching factor and m is the number of prism layers.

These equations are related to each other and used together to calculate the parameters necessary for the prism layers.

2.5.1.3 Checking the mesh quality

Before running the simulation, it is important to validate the mesh of the problem geometry. Simcenter STAR-CCM+ has seven main mesh quality metrics: face validity, cell quality, volume change, cell skewness angle, chevron quality indicator, least square quality, and cell warpage quality.

Face validity: "*The face validity is an area-weighted measure of the correctness of the face normals relative to their attached cell centroid.*" [8][p. 3167] The Face validity is put on a scale from 0 to 1 where 1 is a perfect cell and everything below is considered bad and should never go below 0.5.

Cell quality: "*The cell quality metric algorithm is based on a hybrid of the Gauss and least-squares methods for cell gradient calculation methods.*" [8][p. 3167] The Cell quality is put on a scale from 0 to 1 where 1 is a perfect cell and everything below 1E-5 is considered bad.

Volume change: "*The volume change metric describes the ratio of the volume of a cell to that of its largest neighbor.*" [8][p. 3168] The Cell quality is put on a scale from 0 to 1 where 1 is a perfect cell and everything below 0.01 is considered bad.

Cell skewness angle: "*This skewness measure is designed to reflect whether the cells on either side of a face are formed in such a way as to permit diffusion of quantities without these quantities becoming unbounded*" [8][p. 3169]. The cell skewness angle is an angle where a value above 85° is considered bad.

Chevron quality indicator: "*Chevron cells are pairs of thin slender cells which meet at a common face at an angle such that the line joining the cell centers does not pass through the common face*" [8][p. 3170]. On a binary scale chevron cells marked as 1 are considered bad.

Least square quality: "*This field function is an indicator of the quality of a cell, using the physical location of a cell centroid relative to the cell centroid locations of its face-neighbors*" [8][p. 3170]. The cell quality is put on a scale from 0 to 1 where 1 is a perfect cell and everything below 10^{-3} is considered bad.

Cell warpage quality: "*Cell warpage quality identifies thin and warped cells. These types of cells can cause issues for the flow solver, especially for high-fidelity simulations such as LES/DES and acoustics, where minimal dissipation is required*" [8][p. 3171]. The cell quality is put on a scale from 0 to 1 where 1 is a perfect cell and everything below 0.15 is considered bad.

2.5.1.4 Model selection and flow properties

The selection of the simulation model is based on the physics of the problem [7]. Firstly, a simulation type best fitted for the problem is chosen [7]. This tells the simulation how the flow should react according to its physical state. Secondly, the parameters of interest are determined [24]. It is important to understand the problem to define the parameters correctly and get accurate data from the results [24].

This study will be using the so-called *Reynolds Stress Transport Model* (RST) when solving the URANS equations. The RST models are higher-level turbulence closures and can account for complex interactions in turbulent flow fields [28].

2.5.1.5 Initial and boundary conditions

The final part of the pre-processing is to give the problem initial conditions and boundary conditions [7]. This is done in order to complete the mathematical model and it enables the flow to enter or leave the computational domain [8][p. 8479].

Boundary conditions define how the solver treats the solved-for quantities around the perimeter of the computational domain [8][p. 9837]. At the stagnation inlet for incompressible flows, Bernoulli's equation is used when relating total pressure, static pressure, and velocity magnitude, which also is the values that Simcenter STAR-CCM+ computes at the boundary faces [8][p. 8480].

The initial conditions specify the initial field data for the simulation [8][p. 9836]. The model requires the primary variables to be set at sensible values throughout the computational domain at the start of the simulation.

2.5.2 Simulation

During the simulation part, the governing equations are solved over the geometry [7]. When solving the governing equations, which are types of partial differential equations, CFD uses discretization methods [23]. Simcenter STAR-CCM+ mainly uses the *Finite Volume Method* (FVM) for fluid flows, which also will be used in this study [8][p. 46].

2.5.2.1 Finite Volume Method (FVM)

FVM is as stated above the most common type of discretization method used in CFD, as it has advantages both in memory usage and solution speed [23]. It is a numerical method and solves the partial differential equations used in fluid dynamics [29]. The first step includes dividing the domain into a finite number of elements, also known as cells. The variables chosen are then put in the centroid of these cells, before integrating the differential equations over each of the elements. To get the discretization equation, interpolation profiles are assumed between the centroids to get the variation of the variable of interest [29].

2.5.3 Post-processing

Post-processing is a crucial part of CFD, as is it here the results are interpreted and validated. Plots, graphs, and other relevant data are here extracted and analyzed for design optimization and conclusions [7]. Simcenter STAR-CCM+ provides three types of post-processing objects; Reports, Plots, and Scenes [8][p. 6804]. For each of the above stated objects, one typically chooses the parts, regions, or surfaces from which the simulation data is extracted [8][p. 6804].

2.6 Data from reports

To get a better understanding of which angles are optimal, data have been collected from multiple sources experimenting with winglets on wind turbines.

2.6.1 Report: *Aerodynamic investigation of Winglets on Wind Turbine Blades using CFD*

In a report by Jeppe Johansen and Niels N. Sørensen, different designs of winglets were tested on a wind turbine using CFD. The winglets had a constant height of 1.5% of the rotor radius together with a constant cant angle of 90°. Additionally, the rotor radius was also kept constant during all simulations. However, the study had different twist angles and the direction of the winglets was changed. The results of interest is shown in the table below [20].

Table 2.1: Results from winglet 1.5 % of the blade radius at different wind speeds. The cant angle is set at 90° and the twist angle at 0° towards the pressure side.

	6 [m/s]	**8.5 [m/s]**	**10 [m/s]**	**12 [m/s]**
$\mathbf{0.015 \times R}$	1.42 %	0.60 %	0.90 %	1.04 %

2.6.2 Report: *Numerical study of effect of winglet planform and airfoil on a horizontal axis wind turbine performance*

A. Farhan, A. Hassanpour, A. Burns, and Y. Ghaffari Motlagh conducted CFD experiments on winglets with different airfoils. The base model turbine had two blades and a rotor radius of approximately 5 meters. They tested different lengths, cant angles, and wind speeds for two different airfoil designs. All simulations had a 0° twist angle. The airfoil design most akin to the one used in this report was the S809 airfoil. Winglets in this report are facing the suction side of the blade [30].

Table 2.2: Results from winglets with varying heights at different wind speeds. Over half of the table is for the cant angle set at 90° and the under half is for the cant angle at 45°, both towards the suction side.

90° cant angle	**5 [m/s]**	**7 [m/s]**	**10 [m/s]**
0.05 [m]	3.5 %	5.0 %	5.4 %
0.10 [m]	3.8 %	6.3 %	6.7 %
0.15 [m]	5.3 %	9.5 %	7.1 %
45° cant angle	**5 [m/s]**	**7 [m/s]**	**10 [m/s]**
0.05 [m]	5.1 %	7.0 %	9.1 %
0.10 [m]	5.1 %	6.8 %	9.4 %
0.15 [m]	5.4 %	7.4 %	9.8 %

2.6.3 Report: *The effect of using winglets to enhance the performance of swept blades of a horizontal axis wind turbine*

Mohamed G Khalafallah, Abdelnaby M Ahmed, and Mohamed K Emam simulated a wide range of winglet configurations. The cant angles examined were 20°, 40°, and 60°. All cant angles were simulated with three different twist angles -2°, 2°, and 10°. In addition, variations in winglet orientation between the pressure and suction sides are investigated. During all simulations, the wind speed, expressed in tip speed ratio, was held constant at a value of 6 m/s [31].

Table 2.3: Results from winglets with varying heights at different wind speeds. Over half is for the cant angle set at 90° and the under half is for the cant angle at 45°, both towards the suction side.

Cant/Twist	**-2°**	**2°**	**10°**
20° (pressure)	0.20 %	1.05 %	1.39 %
20° (suction)	0.26 %	0.38 %	0.28 %
40° (pressure)	0.33 %	0.66 %	0.60 %
40° (suction)	1.69 %	1.72 %	0.84 %
60° (pressure)	-0.46 %	-0.33 %	-2.01 %
60° (suction)	1.64 %	1.75 %	0.19 %

3
Method

In this chapter, the methodology regarding this project is presented. The setup of the CAD models will be explained, alongside with the setup and execution of the CFD simulations.

3.1 Research

To get a better understanding of how to determine a wind turbine's efficiency qualitatively, research on previous studies in the field was carried out. By evaluating how others have measured a wind turbine's output power and comparison between different models, the group could use their methods as inspiration to further develop their own. Moreover, published papers and other relevant sources of information were used to get an understanding of the aerodynamics of wind turbines and how they generate power.

To gain knowledge about the simulation program (Simcenter STAR-CCM+), the group mainly used tutorials published online together with a user-guide written by Siemens. By following experienced users in the field, the group could gain knowledge of how the program works and behaves. In addition, consultations with a supervisor were continuously held during the process.

3.2 Setup of CAD models

When designing and setting up the models in the software programs, SolidWorks was first used to construct the wind turbine and the different winglets. All models used in the making of this report were based on a ready-made model from grabcad.com [32]. The model consists of three parts; the blade, the hub, and the tower. The blade was cloned during assembly in order to get three blades. The constructed winglets were later added to the modified blades and were designed using the existing profile of the blade.

3.2.1 Base model

As previously mentioned, a ready-made wind turbine model was selected. This file served as a base for the project. However, before using the model several changes were made. These changes are described in the following subsections and they were

made in order to increase the efficiency of the simulation and to remove errors in the meshing process. More on this under Section 3.3.2.

3.2.1.1 Geometry

The blades in the model are made using the *loft* function on several curves. The way this was implemented in the original model led to the blades being hollow. When applying a mesh to this model, it also created a mesh on the inside of the blades inducing a great amount of unnecessary workload on the simulation. Fixing this issue was an easy undertaking since the blade where hollowed out by subtracting a scaled-down version from the blade itself. Removing this subtraction and scaled-down version of the blade made it solid.

The same method as stated above was applied to the hub since it too was hollow. In addition, the hub also had a few crevices that were filled in to create continuous geometries for the meshing and to make sure the assembly resulted in a solid part without any ”floating” parts. This is illustrated in Figure 3.1 below.

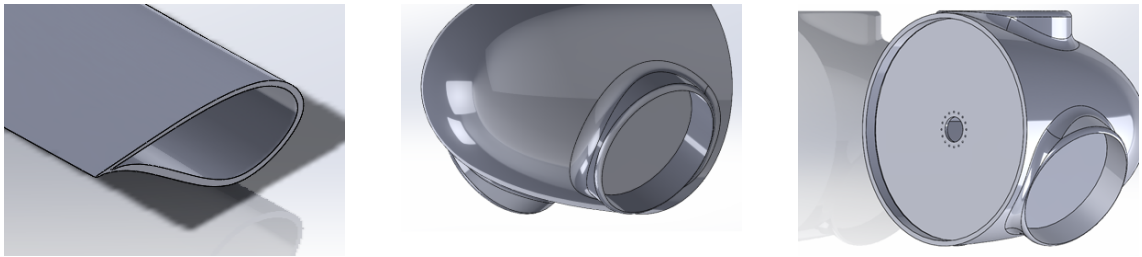

(a) Original model

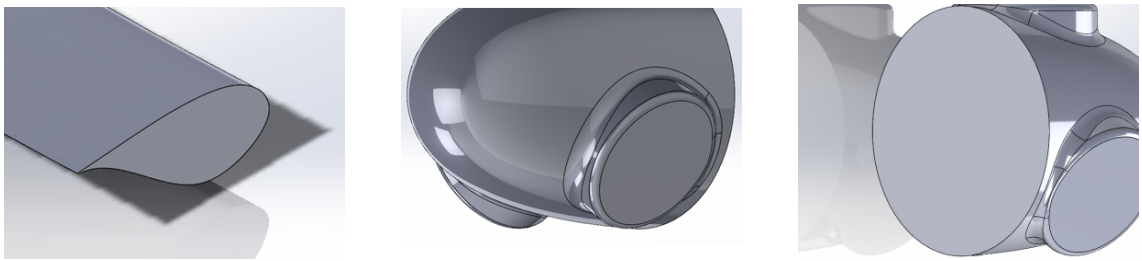

(b) Model used in simulation

Figure 3.1: Cross-section of the wing (left), the connection point for the wing on the hub (middle), and back of the hub (right) before and after solidification.

3.2.1.2 Pruning

There were some parts on the original blade design that were unnecessary for the ends which were removed in order to save computing power. The original model had make-shift screws attached to them, presumably to help with fixing the blades to the hub when assembling the entire turbine. These screws were removed entirely from the model since they served no purpose in the context of this study, see Figure 3.2. There was also a slight change made to the geometry of the last *curve* feature

to resolve issues with the geometry during meshing. Furthermore, the tower was removed before the the turbine was transferred to CFD software. The tower was deemed unnecessary for the simulation and removing made simulation simpler and more accurate.

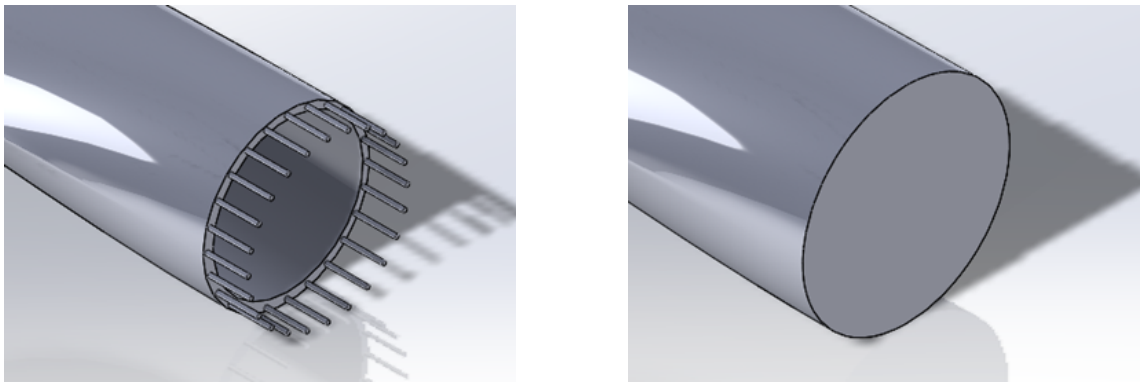

Figure 3.2: Base of the wing, original model with screws (left), and model used for simulation (right)

3.2.1.3 Scaling

Since the model was originally full-sized with a radius of 47.6 meters it was decided to use a scaled-down version to shorten computation time. This was achieved by applying SolidWorks' *scale* function on the parts and reassembling the model. To keep the Reynolds number selfsame and avoid getting a compressible airflow, the model was scaled to 60% of the original size (see Figure 3.3).

Figure 3.3: Original model (right) and the scaled-down version (left) side by side

3.2.2 Winglet models

To create the winglets, an outline of the blade-tip cross-section was created and later duplicated onto reference planes. Using the *loft* function on the outlines the shape of the winglet was automatically created. Thence, the tip of the winglets was created using the *dome* function. The cant angles used for the different winglet configurations was 90°, 60°, and 45°. These angles were chosen by taking inspiration from previous studies.

3.2.2.1 Geometric delimitations

Since the study aims to compare how different cant angles affect the aerodynamic efficiency, the blade would increase in length (turbine radius) as the angle decreases. It was decided that the radius of the turbine should be kept the same. This was achieved by adding a ”buffer” area between the winglet and the rest of the blade. This buffer was shortened by the same measurement as the winglet would increase the radius. Illustrated in Figure 3.4.

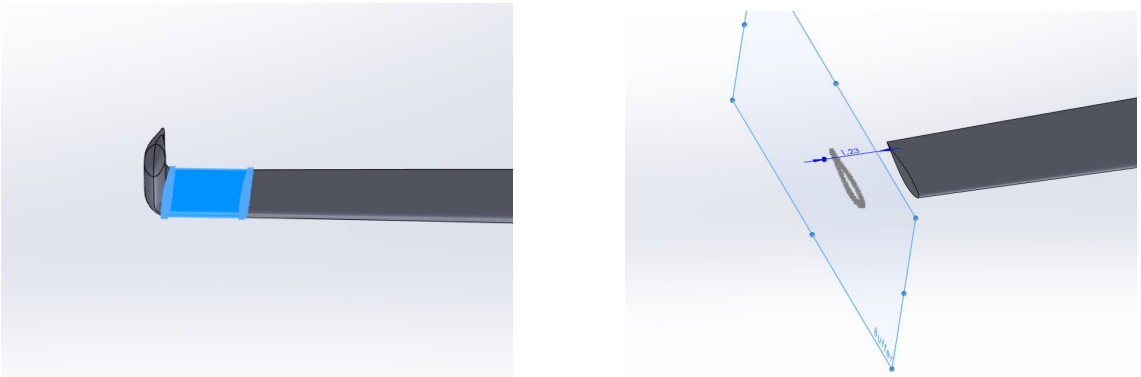

Figure 3.4: W90 blade with highlighted buffer are (left) and reference plane used to create and adjust said area.

The length of the winglets was also kept constant for every angle. The length of the winglet refers to the measurement illustrated in Figure 3.5.

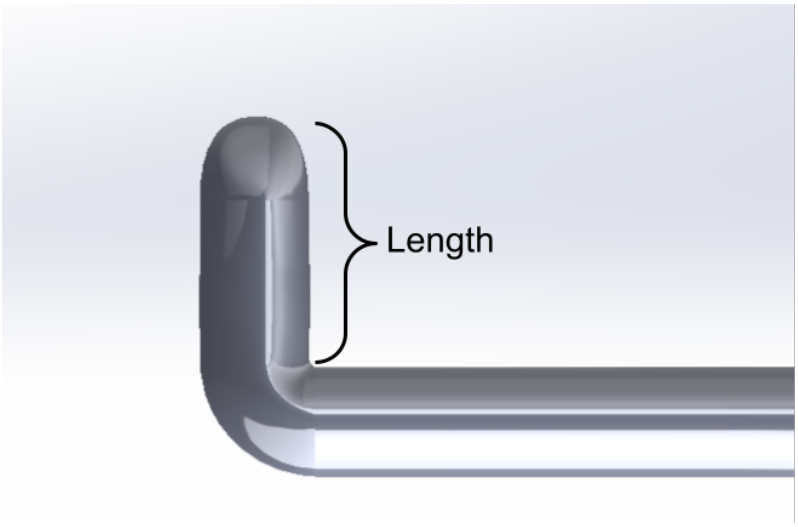

Figure 3.5: W90 blade with ”length” indicator

3.2.2.2 Geometry

To shape the winglet, several well-placed reference planes were created. These allowed for easy adjustment of the different measurements when designing the winglets, such as the aforementioned buffer area.

Seven reference planes were used to create the winglet, four of which were used to restrain the shape of the winglet. The remaining three were used to get the right distances for the measurement (see Figure 3.6). For clarity, the last three will be referred to as the buffer-, toe- and sweep-planes. The buffer plane dictates the length of the buffer area. The toe plane is placed tangent to the tip of the blade in order for the base to be correct. Lastly, the sweep plane dictates the length of the winglet. On each of these planes, there is a sketch of the winglet cross-section. The offset between the sketches on the toe and sweep planes dictates the cant angle.

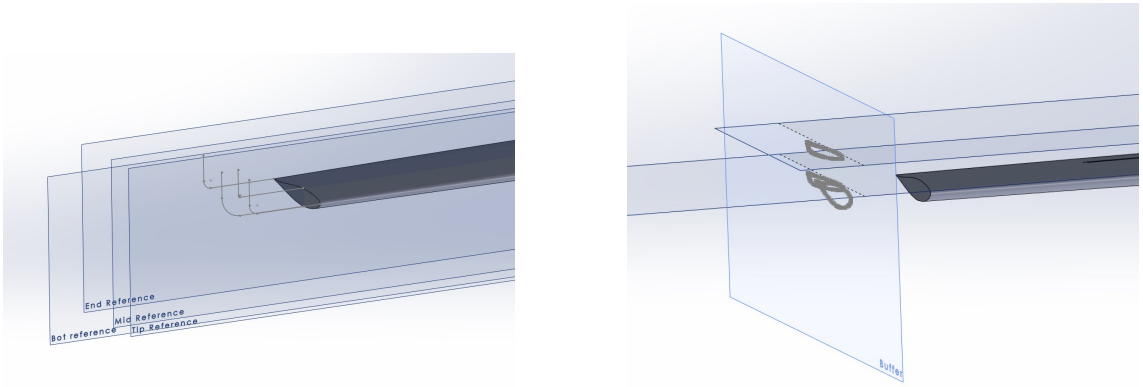

Figure 3.6: W90 blade reference planes with respective geometries. All reference geometries and their reference planes (left) and buffer, toe, and sweep planes with winglet cross-sections (right)

As mentioned previously, the *loft* function was used to create the winglet geometry with four of the reference planes containing reference geometries used to restrain the shape. When applying the *loft* function without these reference geometries the shape becomes more ”fluid” (see Figure 3.7). The reference geometries are used by SolidWorks as guidelines for the geometry and ensure a more structured shape for the winglet.

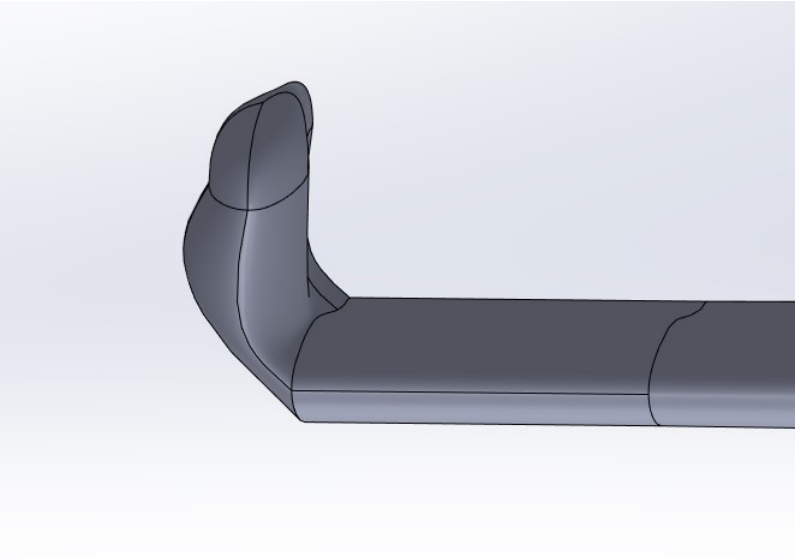

Figure 3.7: W90 blade without reference geometries

Lastly, also previously mentioned, the *dome* function is used to create the rounded shape at the tip of the winglet. This creates an extra height on the winglet which is offset by lowering the sweep-plane. In the models where the winglet is not at a right angle compared to the blade, a part of the winglet was removed for the dome to be at the same angle as the winglet. This was done instead of angling the plane.

3.3 CFD

The CFD simulations were performed using the program Simcenter STAR-CCM+ by Siemens (version 18.06.006). The simulation was first set up for the standard turbine, without the winglets, at a wind speed of 10 [m/s]. Further, the tip speed ratio was set to $\lambda = 6$. This number was chosen due to previously done research, suggesting this value. Then, after validation of the results, the setup was applied to the rest of the different winglet configurations and wind speeds (note, the tip speed ratio were held constant for all models and wind speeds). The process of setting up the first simulation, for the standard turbine, will therefore only be explained since the setup methodology looks the same with the only difference being a switched model and minor tweaks in the parameters. Down below, the pre-processing part is described.

3.3.1 Geometry validation and defining domains

The CAD file was imported into Simcenter STAR-CCM+ in the CAD geometry editor as a step file. The CAD-model consisted of four different sub-bodies; "Blade 1", "Blade 2", "Blade 3" and "Hub". These together were assigned to a single geometry part. When transferring the CAD model to the part, the tessellation density was made "very fine". This was done to prevent surface errors such as non-manifold edges and vertices.

3.3.1.1 Definition of computational domain

The first step in setting up the simulation after importing the CAD model and deriving the geometry part was to define the computational domains and sort out the surfaces. A surface wrap was made over the geometry part, using the *surface wrapper* tool. For the wrapping parameters see Table 3.1. The wrap surfaces were then sorted and renamed using the *split by patch* tool resulting in four separate surfaces; "Blade 1", "Blade 2", "Blade 3", and "Hub". The wrap then became the part that was going to be used as the wind turbine model in the simulations. The reason for this was to eliminate the last of the intersecting surfaces still present in the geometry part, and thus prevent errors in later meshing stages.

Table 3.1: Surface wrapper parameters

Surface Wrapper - Default Controls	
Parameter	**Setting**
Base size	1 m
CAD Projection	Activated
Target surface size	10% (Relative to base)
Minimum surface size	0.1% (Relative to base)
Surface curvature	Deactivated
Volume of interest	External
Smallest disconnected surface	1000 (num. faces)
Feateure angle	30°

The technique used for achieving the rotating motion combined with the stationary flow was the so-called *Sliding mesh technique*. The reason this specific method was used was due to it being recommended on the Siemens website by the Siemens community for fan/propeller style simulations, with the main advantages of being simple yet very effective in handling mesh motions [33]. The technique involves the use of two separated fluid/computational domains connected via an interface following the recommendations from the Siemens community. A visualization of this can be seen in Figure 3.8.

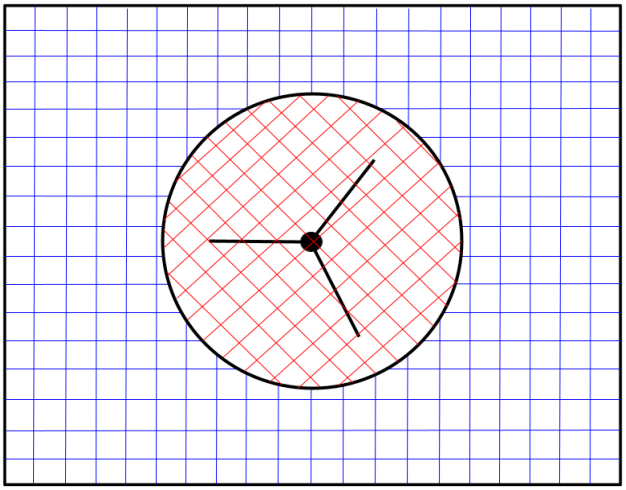

Figure 3.8: Visualization of the sliding mesh technique with two separated domains (including a wind turbine)

The first fluid domain created was the *Rotating domain*. A cylinder part was placed around the wind turbine blades. The surface of this part was kept to a single surface, as seen in Figure 3.9.

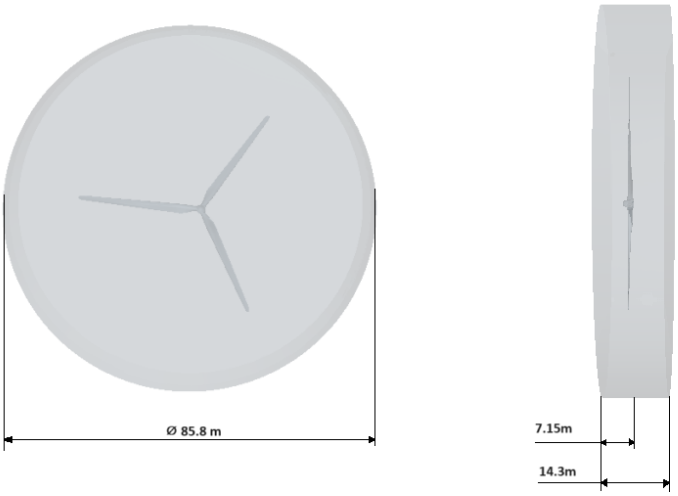

Figure 3.9: The Rotating domain around the wind turbine

The second domain created was the virtual wind tunnel where standard stationary flow is applied. This domain was made by creating a block part with the wind turbine and a rotating part inside of it (see Figure 3.10). The surface of this part was then split into separate surfaces for each comprising wall. These were later to become the virtual wind tunnel boundaries; ”Top”, ”Bottom”, ”Side 1”, ”Side 2”, ”Inlet”, ”Outlet”, and the ”inner rotating part”. These were later used when assigning the virtual wind tunnel to a region.

Figure 3.10: The virtual wind tunnel

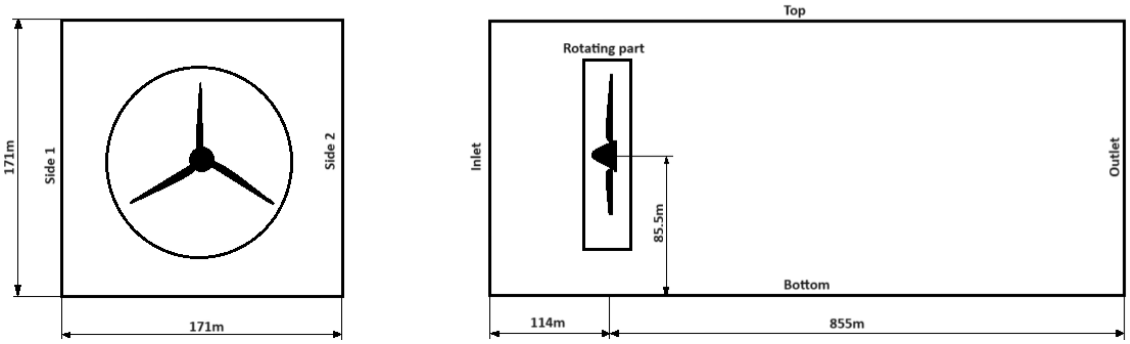

Figure 3.11: Wind tunnel dimensions

For the dimensions of the two created parts see Figure 3.9 and 3.11. These dimensions were chosen large enough mainly to ensure the inclusion of the full wake. But they were also inspired to be proportional to NASA's physical wind tunnel and their test with a ten meter diameter wind turbine [34].

Using the *boolean subtract function*, the next step in deriving the two fluid domains was first to subtract the wind turbine from the cylindrical rotating part. The rotating part was then also subtracted from the wind tunnel block to separate the two domains. These two derived subtracts finally became the two separated fluid/computational domains. The subtracted rotating part was renamed "Rotating subdomain" and the subtracted wind tunnel was renamed "Virtual wind tunnel". In Figure 3.12, a geometry scene with both the final computational domains is displayed (Note that the cylinder located on the inside is the Rotating subdomain and the outer square is the Virtual wind tunnel).

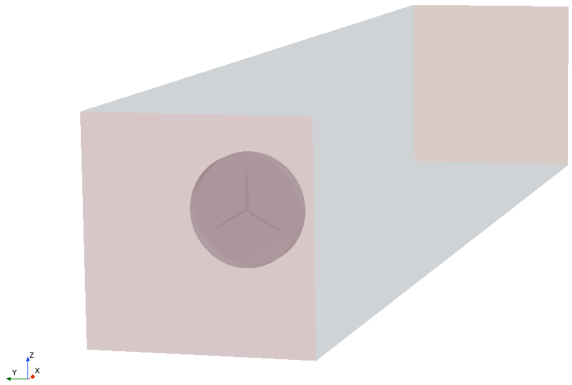

Figure 3.12: The two final computational domains, "Rotating domain" and "Virtual Wind Tunnel"

3.3.1.2 Definition of regions

Two regions were created by assigning the virtual rotating part (VRP) and virtual wind tunnel (VWT) to a region respectively. Following the instructions for the sliding mesh technique from the previously mentioned Siemens community, an interface between the cylindrical "Rotating subdomain" surfaces in both regions was created. This was done to make sure that the two regions interacted correctly. For the interface, the *Direct Intersector* was set to Topology based, and *Close Adjacent Cells* were activated. Also, as suggested by the Siemens community, due to the use of one single boundary for the whole interface containing all the surfaces of the cylinder, the option *Match Outer Perimeter* was applied.

3.3.2 Mesh generation and validation

As stated in Section 2.5.1.2, a mesh is a network of points connected by edges to form triangles. This network represents a coarse version of the surface as simulating down to every molecule would be extremely computationally costly. Down below follows a description of the mesh setup.

3.3.2.1 Parameters for mesh generation

When performing simulations, especially those involving turbulence, there is not a universally defined set of parameters to follow [8][p. 4428]. The Simcenter STAR-CCM+ user-guide provides guidance and recommendations, which were supplemented by insights from YouTube tutorials demonstrating wind turbine simulations. For the volume mesh, a quadratic *Trimmed cell mesher* was used, as it is recommended for external aerodynamic flow by the Siemens community [35]. However, the group did not strictly adhere to a predefined tutorial or parameter set to create the specific wind turbine model used in this study. Instead, certain parameters were determined through a process of trial and error, involving meshing followed by quality checks. A more comprehensive outline of the mesh setup and specifications can be found in Appendix A.1. It is worth noting that parameters not addressed in

the specification were maintained at their default values.

A wake refinement was also incorporated during the meshing process, specifically in the ”VWT” mesh, under ”Volumetric Control” (see Appendix A.1). This refinement was achieved by creating a new cylinder part positioned behind the rotating part, featuring an identical radius but extending 457.6 meters downstream, as illustrated in Figure 3.13.

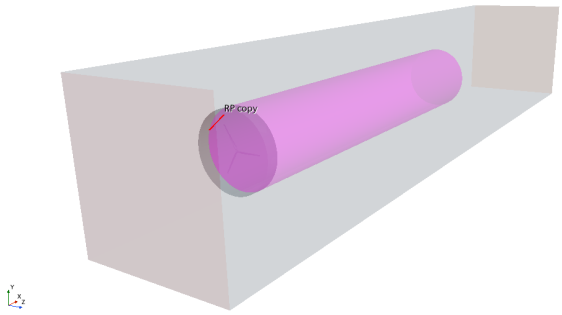

Figure 3.13: A visualization of the wake refinement part

3.3.2.2 Meshing prism layers

As stated, this study used prism layers in the boundary to get a finer mesh and a boundary layer of better quality. Therefore, a calculation of the parameters from the equations in section 2.5.1.2 was performed for both the base of the blade and the tip. The smallest FLT and the largest δ are the desirable values. The smallest FLT is found at the highest velocity and the largest δ is found at the lowest velocity. From these, the Re_C for the FLT was based on the tip of the wing, and the Re_C for the δ was based on the Re_C from the base of the blade.

The wind turbine radius (R), chord length (C), and kinematic viscosity (ν) remained constant across all wind speeds. However, variables such as the chord-based Reynolds number (Re_C), wind speed (V_∞), and rotation speed (ω) varied depending on the selected wind speed. The dimensionless wall distance (Y^+) was set to 200, a value previously used in other wind turbine simulations [36]. Additionally, the stretching factor between the prismatic layers (r) was chosen to be 1.2, falling within the recommended range of 1.05 to 1.2 [27].

The values that were calculated for the mesh were the first layer cell thickness (FLT), the boundary layer thickness (δ), and the number of prism layers (m). The specific values for the different wind speeds can be found in Appendix A.2.

3.3.2.3 Checking the mesh quality

The final mesh of the first setup had 40 chevron cells. This was deemed to be acceptable as the mesh met the other criteria and, compared to the total amount of cells, was a very small part och the mesh as a whole. To minimize the amount

of Chevron cells and to get the mesh to meet the Skewness angle requirement, the minimum cell size was decreased to allow the program to make the cells small enough to adhere to the curvatures of the blades with good cell quality. However, to keep the face count in the recommended range the target cell size was increased.

3.3.3 Definition of physics and boundary conditions

After the meshing was done, the next part of the process was to define the physics and boundary conditions. The full physics continua can be found in Appendix A.3 (Note that the parameters kept as standard are not mentioned). In this simulation, the model used was the elliptic blending Reynolds stress turbulence model (RST) with wall functions. The reason for this was that it was concluded a good choice according to the research [37][38]. Also, since the mesh was based on the use of a higher Y^+ value, the use of wall functions was used. According to the sources mentioned above, the quadratic and cubic variants of the k-ε turbulence model were also recommended. But to balance computational cost with accuracy, the RST-model was chosen.

The boundary conditions are presented in Table 3.2. Using the same Excel sheet as presented in Section 3.3.2.2, the wind speed [m/s] and rotation speed [rps] were defined (for full information, see Appendix A.2). The wind speed was assigned to the physics initial conditions and inlet velocity. The rotation speed was assigned to the rotating region, "VRP".

Table 3.2: Boundaries and boundary conditions

Boundary conditions		
Region	**Boundary**	**Condition**
VRP (Virtual Rotating Part)	Rotation Part	Slip wall
	Blade 1	Wall
	Blade 2	Wall
	Blade 3	Wall
	Hub	Wall
VWT (Virtual Wind Tunnel)	Inlet	Velocity inlet
	Outlet	Pressure outlet
	Top	Slip wall
	Bottom	Slip wall
	Rotation Part	Slip wall
	Side 1	Slip wall
	Side 2	Slip wall

3.3.4 Definition of monitors and stopping criteria

Three reports were created and derived as plots; ”Thrust”, ”Torque”, and ”Power”. The report to the power monitor was set up by first using the Simcenter STAR-CCM+ built-in torque calculator to get the torque report, and then taking that torque times the rotation speed [rad/s] to calculate the power. This was done using an *expression function*.

The maximum run time stopping criterion for the first simulation was set to let the turbine complete three whole rotations before stopping. This was, as will be discussed later in the report, changed to only one rotation after the convergence of the simulation had been validated. The maximum run time was based on the time step, which is the time it takes to rotate one degree, in the solver settings. This time step was derived by taking one divided by the rotation speed in [rps]. The temporal discretization was set to the second degree, which also was made in the solver settings.

3.3.5 Simulation

The simulation was done through the National Academic Infrastructure of Supercomputing in Sweden (NAISS) to get the simulations done in a reasonable time and with a good level of accuracy. Through NAISS, access was given to a supercomputer that was used to run our simulations. Computing on the supercomputer was done in parallel instead of in serial which is done on standard computers.

3.3.5.1 Validation of setup and simulation

To validate the simulation setup and test its accuracy and convergence, several factors were analyzed. First, the setup was run multiple times, each time with a finer and finer mesh. The mesh refinement was done by simply reducing the base size. Three different levels of base size refinements were made; a base size of 8 meters, 6 meters, and 4 meters. By looking at the thrust, torque, and power plots, a conclusion was made that the difference between the results of the 6 meter base size and the 4 meter base size was satisfactorily small. Therefore, to save computational cost, the simulation setup with the base size set to 6 meters was deemed good enough. Another factor that was analyzed was the convergence of the residuals in the residuals plot. For a simulation dealing with unsteady and highly turbulent flow, it is often harder to see a convergence in the residuals. But for this simulation, the residuals were deemed okay.

3.3.5.2 Simulation of the different models

After the validation of the simulation setup, the main simulations could be carried out. All three different winglet configurations (with cant angles of 90°, 60° and 45°), as well as the standard blade without winglets, were simulated three times using three different wind speeds respectively. Based on research, the wind speeds were set to 10 m/s, 7.5 m/s, and 5 m/s. Note, that these wind speeds also had to

be scaled due to the scaled turbines and to keep the dynamic similarity. This was done in the previously mentioned Excel sheets, see Appendix A.2. The change in wind speed meant that the required prism layer parameters also had to be changed between the simulations. This caused some of the cell quality parameters, mainly ”skewness angle” and ”chevron cells” to be altered past the ”bad” limit. The mesh was in those cases fine-tuned to minimize this.

Following the initial simulation, it became evident that the power, thrust, and torque output plots stabilized at around the one-second mark or 56% of a rotation. Subsequent simulations of different speeds were run and provided further insights, leading to the conclusion that it was the one-second duration that was needed for the stabilization rather than the 56% rotation.

To be able to run as many simulations as possible, the stopping criterion (maximum run time) were changed to do only one revolution. However, one simulation had to be aborted earlier, which was the winglet configuration with a cant angle of 60° at the wind speed 5 m/s. That simulation had to run for 1.6 seconds before a stabilized value was obtained.

3.3.6 Post-processing

During the post-processing, the data needed was extracted from the simulations that had been executed. The data was then visualized in plots.

Thereafter, scalar scenes of the necessary field functions were created in order to visualize the aerodynamic effects of the different configurations. One scalar scene was made to display the wake created by the turbine. The scalar function on that scene was set to display the velocity magnitude. The other scalar scenes visualized ”total pressure coefficient”, ”total skin friction coefficient” and ”turbulent kinetic energy”.

4

Results and Analysis

This chapter presents the results obtained from different models. The purpose of this study was to investigate how winglets affect the performance of wind turbines.

Three distinct designs of winglets were examined, each featuring varying cant angles and all being pointed towards the pressure side. Additionally, the models were tested under three different wind speeds. The analysis in this chapter will compare the findings of this study with those of previous reports, aiming to validate and explore any similarities. Firstly, a general comparison between the models will be presented.

4.1 General differences

In this section, the output power of the different models at various wind speeds is presented and compared. The flow is assumed to be incompressible, and turbulence is modeled using the Reynolds Stress Transport Model (RST).

4.1.1 Power coefficient

The models featuring attached winglets have cant angles of 45° ($W45$), 60° ($W60$) and 90° ($W90$). Additionally, all winglets are oriented towards the pressure side of the blade. The model without a winglet, which serves as the baseline for comparison with the other models, is referred to below as *Standard*. Table 4.1 presents the power coefficient increase for the various winglet models compared to the standard blade at wind speeds of 5 m/s, 7.5 m/s, and 10 m/s. To get a better visualization of the differences, an overview is shown in figure 4.1.

Table 4.1: Power coefficient percentage compared to the standard blade.

Power coefficient (% increase)			
Wind speed	W90	W60	W45
5 m/s	-4.45 %	-5.30 %	-3.67 %
7.5 m/s	-4.53 %	-7.79 %	-5.50 %
10 m/s	-4.23 %	-5.94 %	-4.03 %

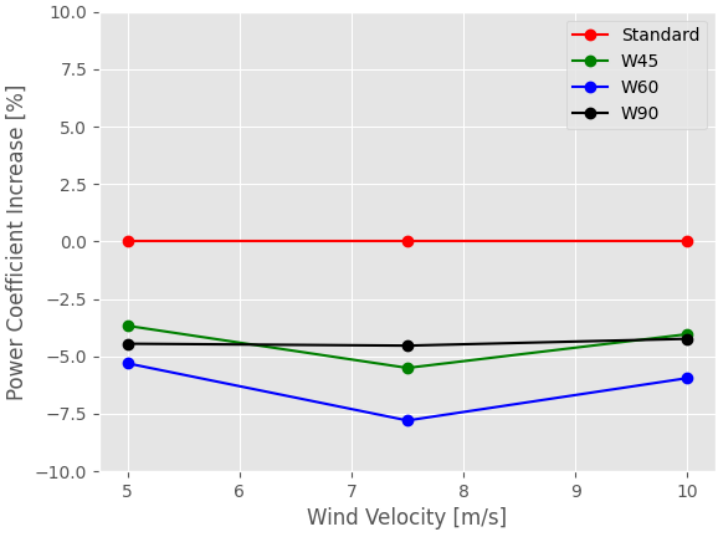

Figure 4.1: Power coefficient increase compared to standard

The presented values indicate that irrespective of the winglet design and wind speed, there is a consistent decrease in the total output power. $W90$ behaved similarly to the standard blade during all wind speeds, while $W60$ and $W45$ followed another pattern. At the wind speeds 5 m/s and 10 m/s, $W45$ had the lowest decrease out of all designs with values of 3.67% and 4.03% respectively. However, at the wind speed 7.5 m/s, $W90$ had the lowest decrease with a value of 4.23%. $W60$ produced the lowest values during all wind speeds, making it the least efficient out of all of the designs.

Overall, the numbers show that the lowest values were obtained at wind speed 7.5 m/s, regardless of winglet design. However, at wind speed 5 m/s, $W60$ and $W45$ had their highest values respectively while $W90$ showed its best performance at the wind speed 10 m/s.

4.1.2 Thrust

When incorporating winglets onto wind turbine blades, it is also of interest to investigate their influence on thrust force. As stated in Section 2.1, the thrust force which is acting perpendicular to the rotor plane, imposes stress on the wind turbine blades and tower. Table 4.2 presents the thrust force exerted by various winglet models in comparison to the standard blade at a wind speed of 10 m/s.

Table 4.2: Comparison of Thrust Forces for Wind Turbine models at 10 m/s Wind Speed

Thrust (T_N)				
Wind turbine model	Standard	W90	W60	W45
Total force [kN]	335	315	310	317
Thrust increase compared to standard [%]	-	-6.02	-7.71	-5.44

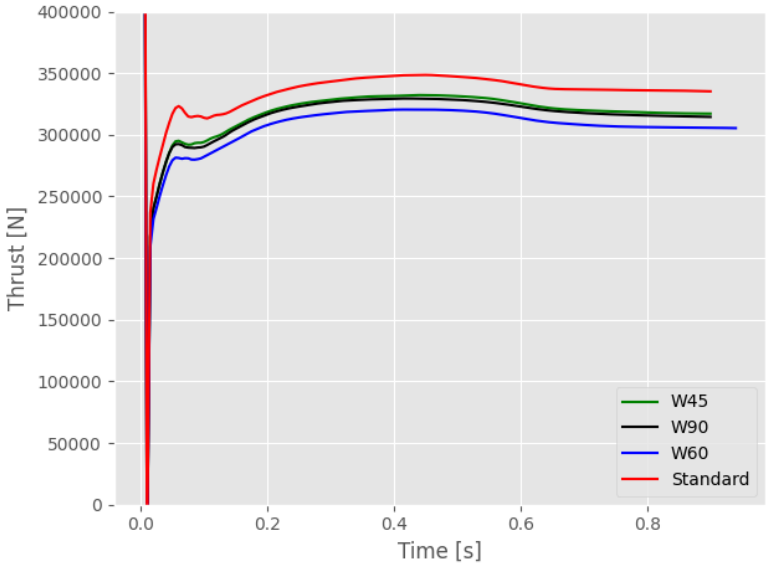

Figure 4.2: Total Thrust force [N]

Looking at Figure 4.2, the total thrust force behaved similarly across all models during the time period. However, across the models with winglets, a decrease in thrust was evident. $W45$ remained closest to the standard blade, with a total thrust force of 317 kN, resulting in a decrease of 5.44% compared to the standard blade. However, $W90$ had a total thrust force close to $W45$, at 315 kN which corresponds to a decrease of 6.02%. $W60$ produced the lowest thrust force, with a value of 310 kN or, in other terms, -7.71% of the standard blades' total thrust force.

4.1.3 Pressure coefficient

To illustrate how the pressure distribution over the blades varies with the different designs, the pressure coefficient was investigated. The pressure coefficient for both the front and back of the wind turbine blades are presented in Figure 4.3. The standard model is compared with W90 and W60 at the wind speed 10 m/s.

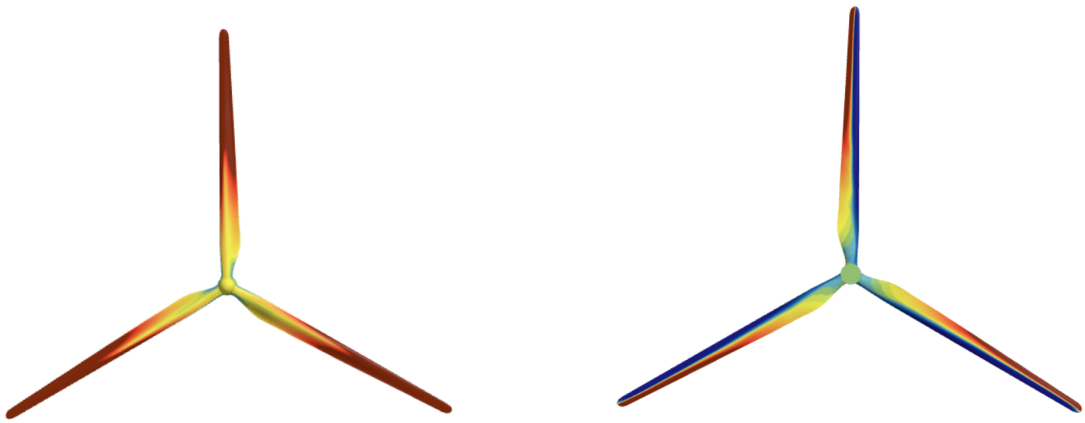

(a) Standard blade, front (left) and back (right)

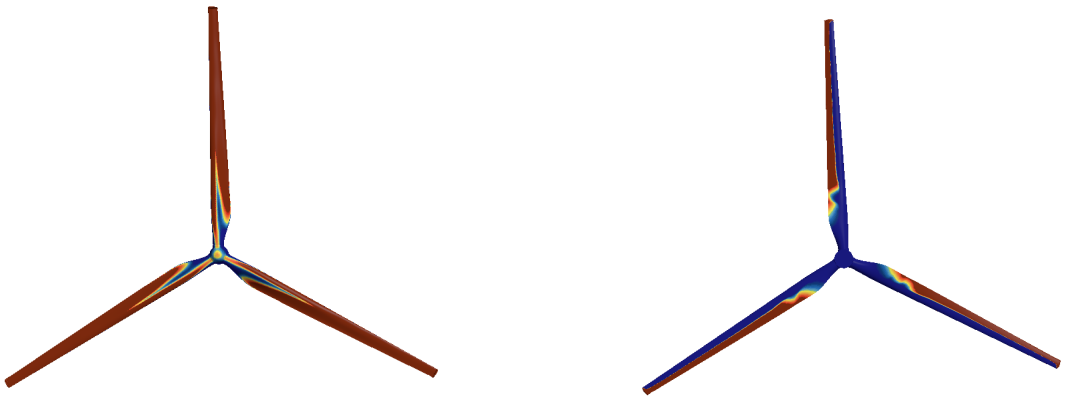

(b) W90 Winglet, front (left) and back (right)

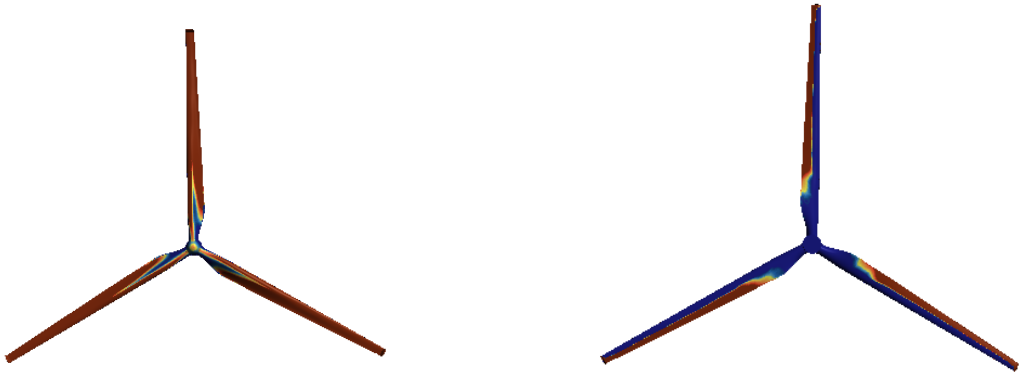

(c) W60 Winglet, front (left) and back (right)

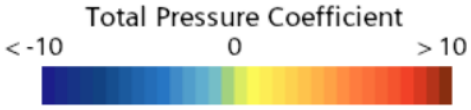

figure continues on next page

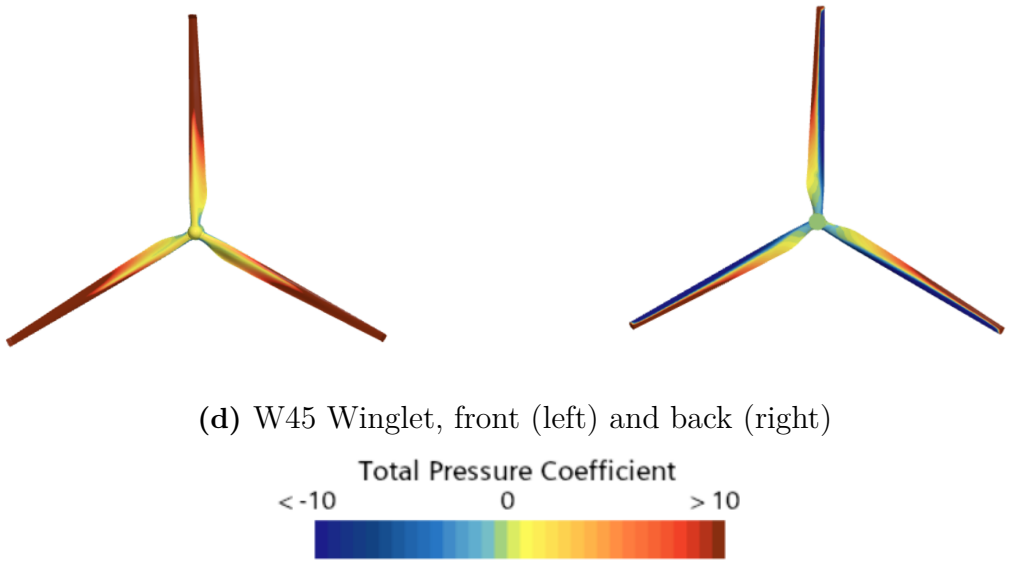

(d) W45 Winglet, front (left) and back (right)

Figure 4.3: Pressure coefficient (C_{pr}) for different winglet designs, and scale, at 10 m/s wind speed.

The plots illustrate that the total pressure coefficient between the winglet designs are very similar. The front side of the blades experiences a high-pressure area except close to the hub. However, the back side of the blades is characterized by a divided distribution of high and low-pressure areas, with a notably larger low-pressure region near the hub compared to the front side. Contrasting these patterns, the standard blade displays distinct features, particularly close to the hub. While the tip of the blades bears resemblance to designs with winglets, the region near the hub exhibits deviations. Specifically, the pressure coefficient for the standard blade in these areas tends to hover around zero, differing from W90 and W60 with values of around -10 respectively. The W45 however, is identical to the standard blade. Moreover, looking at the difference between the winglet configurations and the standard blade, the pressure coefficient tends to increase more rapidly when winglets are added.

4.1.4 Skin friction coefficient

Skin friction coefficient for models with a standard blade, W90 winglet, W60 winglet, and W45 winglet at 10 m/s wind speeds are presented in figure 4.4 below, scale located at the bottom of the figure.

(a) Standard blade, front (left) and back (right)

(b) W90 Winglet, front (left) and back (right)

figure continues on next page

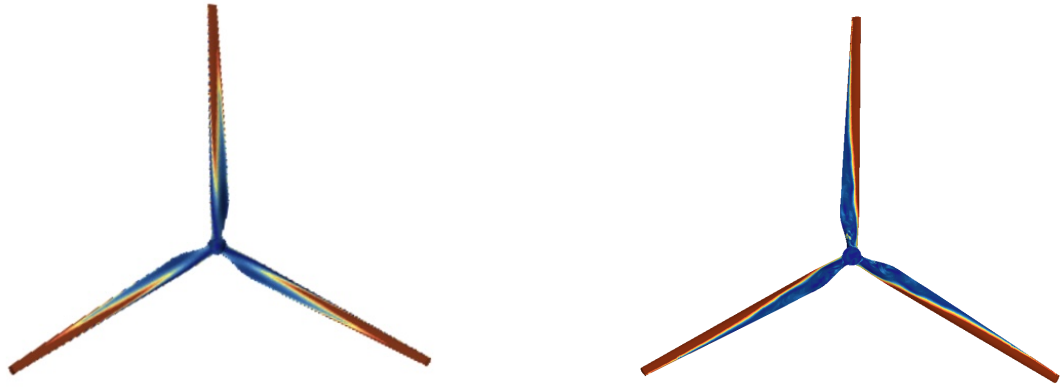

(c) W60 Winglet, front (left) and back (right)

(d) W45 Winglet, front (left) and back (right)

Figure 4.4: Skin friction (C_f) for different winglet designs, and scale, at 10 m/s wind speed

The plots reveal that C_f is very similar for both $W90$ and $W60$, however they both diverge from the standard and $W45$ models by a substantial amount. Looking at the back plots one can see that the high friction region has spread a lot further down and is more developed. In the standard and $W45$ models a large portion of the blade has a high C_f covering approximately half the blade. On the $W90$ and $W60$ models the areas with a high C_f are larger and very similar to each other.

Looking at the plots illustrating the front of the turbine, though the $W90$ results are missing, the results are much the same. However, the magnitude of the difference compared to the standard model is significantly larger. Except for the case of the $W45$ winglet, which is more akin to the standard model with the main difference being a higher C_f at the tip of the blade. In the standard model there are only a few pixels at the tip of the blade displaying maximum skin friction whilst the $W60$ model has dark red areas far down the blade.

4.1.5 Turbulent Kinetic Energy

The TKE for the different winglet configurations are visualized in Figures 4.5-4.7. Note that, due to the turbine being rotated slightly different between the taken pictures, a respective picture of the standard turbine had to be made in order to match the different rotations. This was done to make the result comparable, since each winglet configuration was compared separately to the standard turbine.

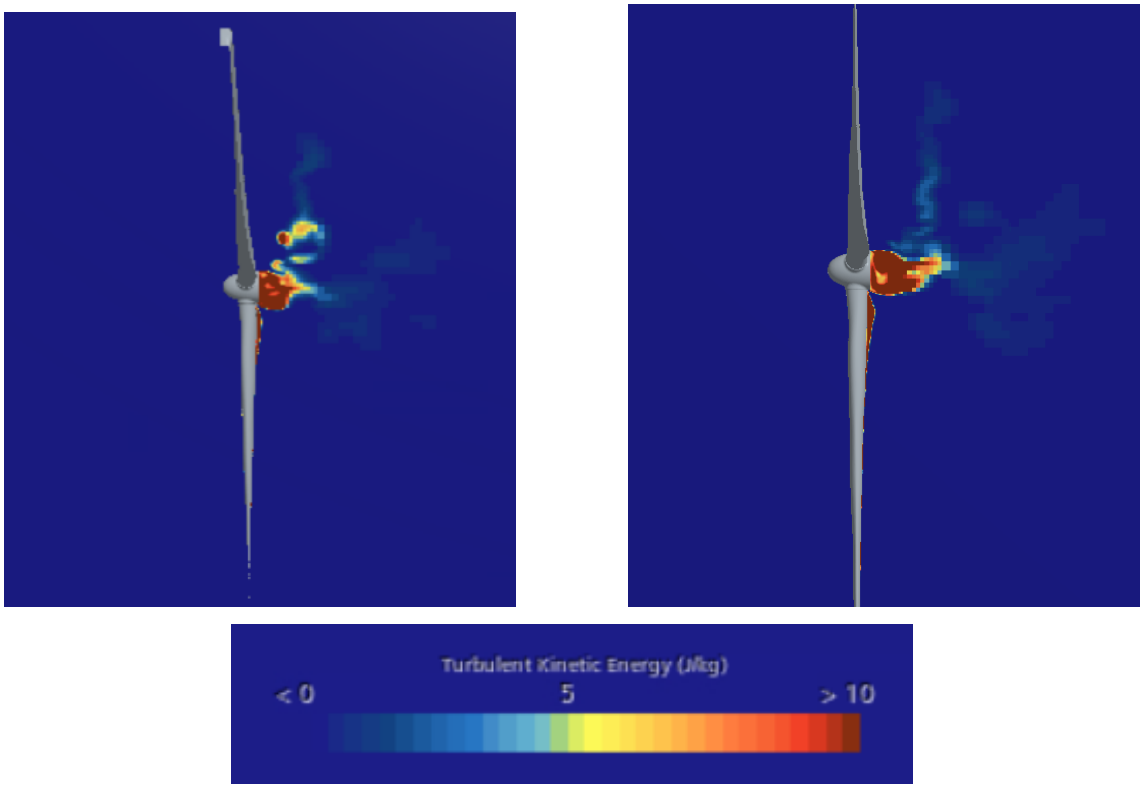

Figure 4.5: TKE for W90 (left), and standard turbine (right)

Starting with the comparison of W90 and the standard blade, no big differences can be seen. Note that the area of interest is the slightly lighter blue parts located behind the wings, since the region behind the hub more has to do with the absence of a tower rather than the effect of the blade. The lasting turbulence seem to be located at pretty much the same distance downstream of the blades.

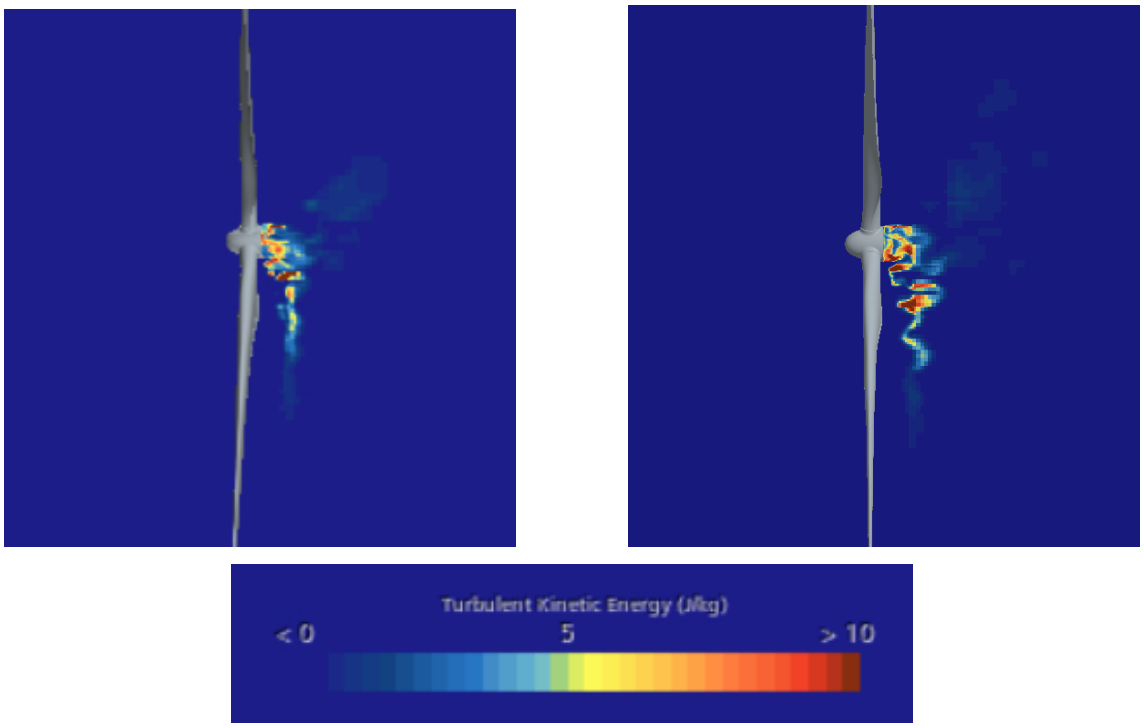

Figure 4.6: TKE for W60 (left), and standard turbine (right)

The same can be said when comparing the W60 configuration to the standard turbine. The eddies of the standard turbine seem to be a little bit larger, however, the difference is not major.

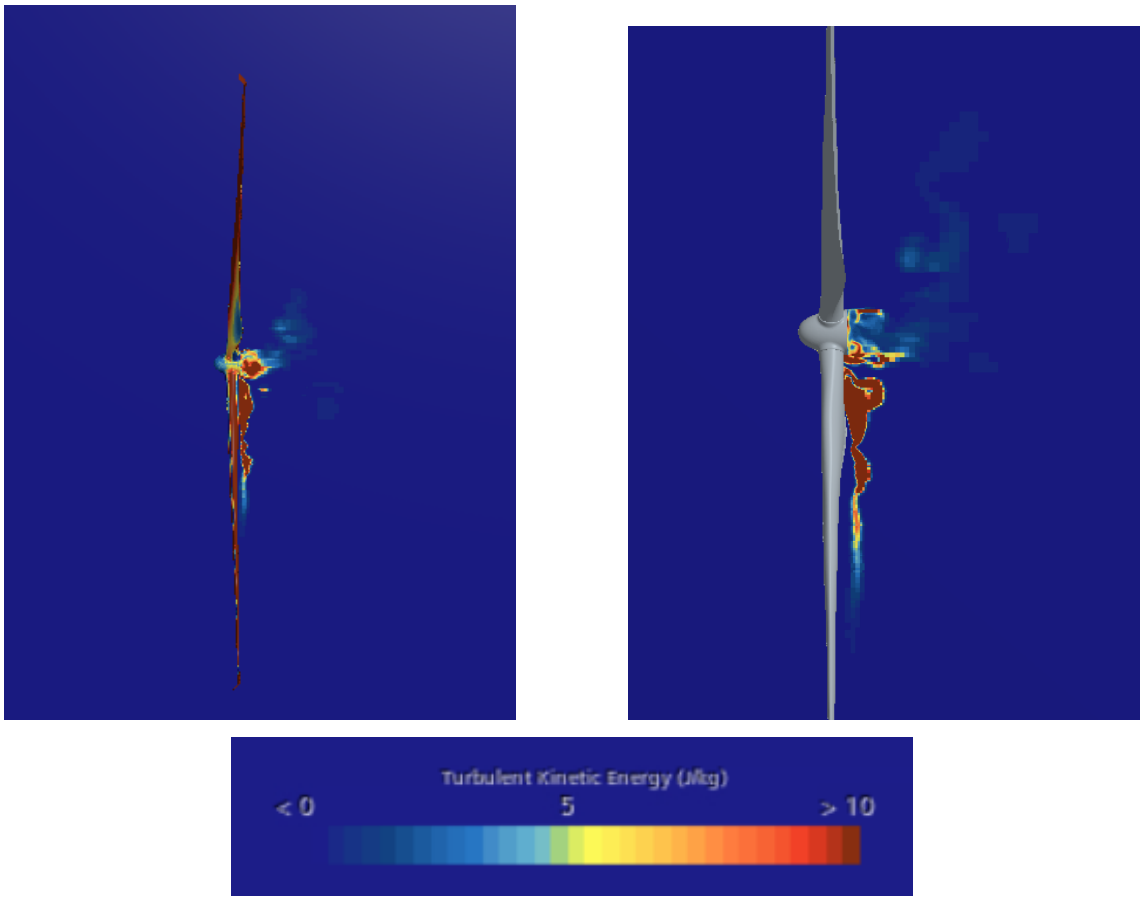

Figure 4.7: TKE for W45 (left), and standard turbine (right)

Looking at W45, the wake look very similar compared to the standard blade (the different colored blades are due to an error when setting up the scene and does not affect the results). However, likewise to the W60 configuration, the turbulence eddies seem slightly larger for the standard turbine compared to the W45 blade. This could hint at a slight turbulence decrease with these winglets. For a discussion about the validity of these images altogether, see Section 5.1.

4.2 Comparison between previous reports

This section examines other reports on the effects of winglets on efficiency in wind turbines. The reports included in these comparisons are *Aerodynamic investigation of Winglets on Wind Turbine Blades using CFD* [20], *Numerical study of the effect of winglet planform and airfoil on a horizontal axis wind turbine performance* [30], and *The effect of using winglets to enhance the performance of swept blades of a horizontal axis wind turbine* [31]. Notably, the focus of these reports primarily revolved around assessing performance in terms of power and thrust. As a result, aspects such as skin friction and TKE were not explicitly addressed. This selective focus underscores why these parameters were not mentioned down below.

Johansen and Sørensen configurations were in contrast to the ones in this project.

The cant angle and height of the winglet were set constant in the compared report, 90° and 1.5% of the blade radius respectively. Meanwhile, in this report, the cant angle has been used as a variable with one configuration being at 90°. In the report of comparison, all configurations with winglets pointed towards the suction side increased their efficiency. However, for the configurations pointed towards the pressure side, the power coefficient decreased at a wind speed of 6 m/s and increased at the higher wind speeds. By evaluating and comparing the results with the ones from this study, the suction side seems to be the preferred side since the efficieny seems to have an positive effect [20].

Farhan, Hassanpour, Burns and Ghaffari Motlagh [30] demonstrate significant enhancement in the power coefficient for all configurations tested in their study. The wind speeds and cant angles closely resemble some of the configurations examined in this report. However, it is noteworthy that all configurations in the report of comparison are oriented towards the suction side, whereas in this report they are oriented towards the pressure side. Similar to the previous compared report, the power coefficient increased for all configurations. This is an further indication that the suction side seems to be the preferable side when adding winglets.

Compared to Khalafallah, Ahmed and Emam [31], the majority of cant angles examined in this report are notably lower. The sole common cant angle, 60°, is utilized in multiple setups in the compared report, along with varying twist angles. Additionally, the winglet was pointed towards both the suction side and the pressure side. In accordance with the compared report, the 60° winglet pointed towards the suction side resulted in a decreased power coefficient. It is worth noting that the decrease in power observed in the results of this study was significantly higher compared to the findings from the compared report. This study further maintained a constant twist angle of 0°, while the configurations in the compared report featured different twist angles. For the winglets pointing towards the suction side, the power coefficient increased. The compared report thus confirms, alongside with the results in this study as well as the other reports, that the pressure side seem to be inferior.

5
Discussion

In this chapter, a discussion regarding this study is presented. Firstly, a comparative analysis of the results is provided. Secondly, reflections regarding the group's methodology are discussed. Lastly, comments on potential improvements for further investigation of the subject are presented.

Note: The comparison between the different designs will solely be based on the results at the wind speed 10 m/s, since they all (except for the power coefficient) are extracted from this specific wind speed.

5.1 Comparative analysis

The overall findings indicate that the addition of winglets pointed towards the pressure side of the blade results in a decrease in power output. At 10 m/s, $W45$ showed values closest to the standard blade with a reduction of 4.03%. Further, $W45$ also demonstrated the lowest decrease in thrust, with a decrease of 5.44% compared to standard. In contrast, $W60$ showed the highest decrease in power output at a decrease of 5.94%, accompanied by the highest decrease in thrust force with a decrease of 7.71%. This observation implies a relationship between power decrease and thrust, where reductions in power are mirrored by corresponding decreases in thrust. Notably, by looking at the power decrease across the different models, the thrust force experienced a larger decrease compared to the power output, resulting in a higher power-to-thrust ratio.

For instance, on $W90$, the power coefficient decreases with 4.23% and the thrust force with 6.02% at wind speed 10 m/s. $W45$ has instead a decrease of 4.03% in power and a decrease of 5.44% in total thrust force. By looking at the difference between the two variables, $W90$ loses more thrust compared to the loss in power in contrast to $W45$, giving it a higher power-to-thrust ratio. Taking these parameters in mind, $W90$ could be a more desirable winglet if the thrust force is a limiting factor.

The results highlight a significant increase in skin friction on the blades due to the presence of winglets on some of the models. A notable observation is that a larger portion of both the front and back of the blade experienced elevated skin friction compared to the standard model for both the $W90$ and $W60$ models. The $W45$ model however did not experience the same level of elevated skin friction. This elevated skin friction, quantified by the coefficient of skin friction (C_f), contributes

to an increase in drag force, consequently leading to a reduction in power output. Interestingly, the differences in C_f between the $W90$ and $W60$ models were minimal, suggesting that the impact of adding winglets, with higher cant angles, is more pronounced than the variation in winglet angle. There seems to be a breaking point between the $W45$ winglet and $W60$ winglet where skin friction drastically increase. These findings could potentially explain the decrease in power output with added winglets, by the fact that the rise in friction drag outweighs any mitigated downwash effect from the winglets. This is supported by the $W45$ model displaying the best results both in power and C_f. However, to draw any final conclusions, additional research is required to comprehensively understand the underlying mechanisms at play. Moreover, it is worth noting that the observed increase in skin friction could also be influenced by the mesh quality. A coarser mesh, as utilized in this study, might exacerbate friction effects due to limitations in CAD and CFD methodologies. This underscores the importance of further investigation into mesh refinement and optimization techniques to ensure accurate simulations and reliable results.

The pressure coefficients for the W90 and W60 configurations showed similar patterns, with slight differences noted. Specifically, the high-pressure zone appeared to extend slightly nearer to the hub in the W60 design. However, it is important to emphasize that the pressure coefficient close to the tip showed similar values for both the standard blade and the winglet configurations. Conversely, as approached the hub area, distinctions became more apparent, particularly in the low-pressure region adjacent to the hub. Here, the standard blade and W45 displayed a pressure coefficient closer to zero, while the winglet designs exhibited values around -10. Closer to the hub, where variations were observed, the winglet design may indeed influence the pressure coefficient, particularly in lowering its values. Further analysis in this area could provide valuable insights into the localized effects of winglets on pressure distribution around wind turbine blades.

An improvement in picture selection for the TKE comparison could be made, but due to limited core-hours and physical time, improving the setup was not possible. To be able to more accurately and extensively compare the effect of the added winglets in this area, the scenes for the TKE could be more optimized. This, by simply making all the rotations of the different iterations uniform, and also aligning the blade with the visualization plane to more clearly show the effects of the wing blades. Maybe also focusing the pictures more on the wingtips would make the TKE more related to the winglets. Regardless of this, some discussion points could be made. The size and location of the turbulence eddies located in the wake behind the blades could still be compared. In the comparison, the turbulence located behind the hub was disregarded due to it not being an effect of the wings, more so an effect caused by the hub itself.

As observed in the comparison with Khalafallah et. al [31], a winglet with the cant angle of 60° tilted towards the pressure side decreased in power. This was consistent with the results in this report. Contrarily, according to Farhan et al. [30], when winglets were tilted towards the suction side, there was an increase in power.

Notably, when visually compared with aeroplanes, winglets are often positioned on the suction side. This observation aligns with the findings, suggesting that a winglet on the suction side may be preferable to one on the pressure side or the standard configuration.

5.2 Reflections on methodology

This section discusses the methodology and inaccuracies of the project. The discussion will explain what could have been improved and thoughts on the project in its entirety.

5.2.1 CAD geometry

This study opted to utilize a CAD model closely resembling a real-world wind turbine. Consequently, considerable time was dedicated to refining the design and tailoring it to suit the objectives of this project. However, it should be noted that this CAD model was not originally intended for CFD simulations. Therefore, modifications were necessary, such as solidifying hollow components and removing extraneous elements like screws. Additionally, adjustments were required to mitigate excessively sharp edges to ensure the mesh quality was optimal.

Looking back, a model specifically designed for CFD simulations would be preferable. Such a model would not only enhance the compatibility with simulation software like Simcenter STAR-CCM+ but also streamline the mesh setup and construction process, reducing complexity and time requirements. Moreover, a smaller model design would facilitate the generation of finer meshes, subsequently lowering computational costs.

A simpler shape better designed for CFD would also help make the CAD process simpler. With the more realistic model used in this report the shape of the winglet was rather complex to achieve since the geometry made the model quite unruly. This could also be affected by the limited CAD experience and knowledge of the members of the group.

5.2.2 CFD

With the limit of 10,000 core-hours, a smaller CAD model would make the simulation run faster to be able to make more simulations and allow for more errors. An underexaggeration of how complicated setting up a simulation was made as we now know that taking a non-simulated CAD with a diameter of about 50[m] and scaling it down 40% was above our ability to produce the result we were hoping for at the start of this thesis. Calculation the C_p for the standard wind turbine gives an average value of 54.1 % over all the wind speeds, with real wind turbine producing around 50 %, our simulations might produce a little high power but not beyond reason. Choosing a smaller and already documented CAD and CFD model, a simpler and

more accurate simulation would have been plausible. This as a result would have given us the time to try more winglet designs and optimize them.

Additionally, an area where improvements could be made is the mesh. Due to the nature of this project, a lot of time was spent learning by trial and error about all the mesh parameters and functions. This did in the end lead to a working mesh, but a mesh done with a larger knowledge about all the functions and possibilities of the program would probably lead to a more optimized mesh in terms of both computational cost and simulation accuracy. Having more control over localized meshing is one example of this. Another example is knowing more about all the different parameters and exactly what they do, as in the case of this project some of the parameters were taken directly from other published simulations and tutorials.

5.2.3 Additional computational values

The initial project scope aimed to incorporate a winglet configuration with an angle of 75 degrees. However, due to time constraints, this aspect of the study had to be omitted. As previously mentioned, the inclusion of additional testing cant angles would have contributed to a more comprehensive analysis of winglet performance.

5.3 Further Research

Previous studies on this subject have suggested that incorporating winglets on wind turbines may potentially enhance power efficiency. However, they also emphasize the necessity for further investigation to draw definitive conclusions regarding performance.

This report focused exclusively on two parameters related to winglet design: height and cant angle. As detailed in Section 2.4.2, three additional angles are typically considered when determining winglet shape and size, although these were held constant in this study. To provide a more comprehensive understanding of the effects of added winglets, future research could incorporate and vary these parameters during geometry design. Additionally, due to time constraints, this project examined only three different cant angles. Expanding this range and including more angles would enable a more comprehensive assessment of this parameter. Furthermore, while this study positioned the winglet toward the pressure side of the blade, investigating the effects of tilting the winglet toward the suction side would be of interest to discern potential directional differences. This would enable a more accurate comparison between the other studies and help, not just assess the validity of the made simulations, but give a more comprehensive answer to the question of whether an added winglet could have a positive effect on a wind turbine.

Alongside winglet design analysis, the project evaluated models under three distinct wind speeds to assess power output. Furthermore, when studying the difference between the pressure coefficient, skin friction coefficient, and turbulent kinetic energy, only the wind speed of 10 m/s was investigated. While the focused analysis at

a single wind speed provided valuable insights, it also posed limitations in fully capturing the broader performance spectrum of the winglet configurations. To address this, future studies could explore a wider range of wind speeds to gain a more comprehensive understanding of how winglets perform across varying environmental conditions. Such expanded analyses would not only enhance the understanding of winglet performance but also provide valuable insights for optimizing winglet designs to maximize power efficiency in wind turbine applications.

Furthermore, the project aimed to investigate whether the application of winglet devices could enhance wind turbine efficiency using CFD. However, as CFD simulations are inherently computer-based, the results provided also lack real-world accuracy. The absence of physical data introduces uncertainty and undermines reliability. For further investigation and research, creating a real prototype tested in a wind tunnel could be used and compared to provide more reliable data.

Additionally, the impact of winglets on parameters such as TKE and skin friction, which have not been extensively explored in the compared reports, presents an opening for further investigation to validate the findings of this study. Additionally, the total pressure coefficient, which was not discussed in the other reports, warrants more research to ensure comprehensive validation. These parameters are essential for a thorough understanding of the effects of winglets on wind turbine performance and can contribute significantly to the advancement of knowledge in this field.

6
Conclusion

Based on the results and analysis, it is concluded that incorporating winglets tilted towards the pressure side decreases the overall performance of wind turbines. However, it is noteworthy that along with the decrease in power output, there is a decrease in thrust force. Moreover, the reduction in thrust force outweighs the decrease in power output, leading to a higher power-to-thrust ratio with the addition of winglets. Since thrust is the primary force the wind turbine must counteract, added winglets may be preferred if thrust becomes a limiting factor. This suggests that pressure side winglets could have a viable application if tower construction reaches a limit on the amount of thrust it can reasonably withstand. In such scenarios, pressure side winglets may effectively enhance the achievable power output.

The winglet designs, while not significantly affecting the pressure coefficient (C_{pr}) except for a lower value around the hub area, raised questions about the reason behind this sudden change. However, what intrigues us most is how various designs, such as winglets pointing towards the suction side of the turbine, would influence the pressure coefficient. The available data indicates minimal variation in C_{pr} values, prompting further qualitative exploration into how alternative designs might perform. This underscores the need for comprehensive studies to better understand the intricacies of winglet configurations and their impact on turbine aerodynamics.

The inclusion of winglets did not yield any noticeable effect on the Turbulent Kinetic Energy (TKE) when compared to the standard blade. Notably, this aspect has not been extensively explored in the compared reports, indicating a gap in research regarding the impact of winglets on TKE. Therefore, further investigation into the effect of winglets on TKE is warranted to provide a comprehensive understanding of their aerodynamic influence.

Adding a winglet to the blade made a clear impact on the skin friction coefficient (C_f), increasing the area of the blade suffering drag forces by a substantial amount. This extra increase in drag force, indicated by C_f, could be one of the factors contributing to the loss of power we see on the turbines. It seems that the increase in drag out performs the reduction in downwash leading to an overall loss of power.

It is of importance to acknowledge that this project has several limitations, which affect the conclusiveness of the results. This study solely focused on investigating the cant angle tilted towards the pressure side. However, further exploration involving additional parameters is necessary to draw any final conclusions regarding added

winglets. Furthermore, additional studies on the selected model for validation are needed to ensure the accuracy of these findings.

In summary, the impact of integrating winglets into wind turbines remains a complex issue. However, drawing insights from both this study and existing literature, it appears that the incorporation of winglets oriented towards the pressure side offers no advantages in terms of power performance. Furthermore, it is important to note that the augmentation in power output may also correspond to a variation in thrust, necessitating further investigation to determine the wind turbine's capacity to accommodate the additional load. This underscores the need for comprehensive analysis and exploration to optimize the design and operational efficiency of wind turbines in practical applications.

Bibliography

[1] F. Wahlström, *Vindkraftsstatistik*, Energimyndigheten, 2024. [Online]. Available: https://www.energimyndigheten.se/statistik/den-officiella-statistiken/statistikprodukter/vindkraftsstatistik/?currentTab=0, Accessed on: 2024-04-22.

[2] C. Laurie, *Technology advancements could unlock 80% more wind energy potential during this decade*, National Renewable Energy Laboratory, 2023. [Online]. Available: https://www.nrel.gov/news/program/2023/technology-advancements-could-unlock-80-more-wind-energy-potential-during-this-decade.html, Accessed on: 2024-03-02.

[3] K. Jayanarasimhan and V. Subramani-Mahalakshmi, "Wind turbine aerodynamics and flow control," in *Wind Turbines - Advances and Challenges in Design, Manufacture and Operation*, Intechopen, Oct. 2022. DOI: 10.5772/intechopen.103930.

[4] N. Hall, *Induced drag coefficient*, NASA Glenn Research Center, 2023. [Online]. Available: https://www1.grc.nasa.gov/beginners-guide-to-aeronautics/induced-drag-coefficient/, Accessed on: 2024-03-14.

[5] Y. Ostovan, "Winglets for wind turbines: An experimental study on aerodynamic performance and tip vortex behavior," Ph.D. dissertation, The Graduate School of Natural and Applied Science of Middle East Technical University, Turkey, 2017. [Online]. Available: http://etd.lib.metu.edu.tr/upload/12621684/index.pdf.

[6] F. M. White, *Fluid Mechanics*, 7th ed. New York, USA: McGraw-Hill Education, 2011.

[7] A. Ali, *CFD Workflow Guide: How to Set Up a Fluid Dynamics Analysis*, Simscale, 2023. [Online]. Available: https://www.simscale.com/blog/cfd-workflow-quick-guide/, Accessed on: 2024-04-25.

[8] Siemens Digital Industries Software, *Simcenter STAR-CCM+ User Guide*. Siemens, 2023.

[9] Cadence Design Systems Inc, *Transient Thermal Analysis*. [Online]. Available: https://www.cadence.com/en_US/home/explore/transient-thermal-analysis.html, Accessed on: 2024-04-29.

[10] Cadence Design Systems Inc, *A Guide to Understanding Turbulent Kinetic Energy*. [Online]. Available: https://resources.system-analysis.cadence.com/blog/msa2022-a-guide-to-understanding-turbulent-kinetic-energy, Accessed on: 2024-05-21.

[11] Simscale, *What is reynolds number*, 2023. [Online]. Available: https://www.simscale.com/docs/simwiki/numerics-background/what-is-the-reynolds-number/, Accessed on: 2024-04-02.

[12] M. Kamran, "Planning and modeling of wind energy systems," in *Fundamentals of Smart Grid Systems*, Academic Press, 2023, pp. 271–298.

[13] A. Kulka, *Pitch and Torque Control of Variable Speed Wind Turbines*, Msc thesis, Gothenburg, Sweden, 2004. [Online]. Available: https://publications.lib.chalmers.se/records/fulltext/174341/174341.pdf.

[14] E. S. Abdelghany, H. H. Sarhan, R. Alahmadi, and M. B. Farghaly, "Study the effect of winglet height length on the aerodynamic performance of horizontal axis wind turbines using computational investigation," *Energies*, vol. 16, D. Astolfi, Ed., 2023. [Online]. Available: https://www.mdpi.com/1996-1073/16/13/5138, Accessed on: 2024-03-14.

[15] L. A. M. Tossas and S. Leonardi, *Wind Turbine Modeling for Computational Fluid Dynamics*, National Renewable Energy laboratory, 2013. [Online]. Available: https://www.nrel.gov/docs/fy13osti/55054.pdf, Accessed on: 2024-03-15.

[16] M. H. Ranjbar, S. A. Nasrazadani, H. Zanganeh Kia, K. Gharali, *Energy Equipment and Systems Reaching the betz limit experimentally and numerically*, 2019. [Online]. Available: https://www.energyequipsys.com/article_36563.html, Accessed on: 2024-03-10.

[17] Center for Sustainable Systems, University of Michigan, *Wind energy factsheet*, 2023. [Online]. Available: https://css.umich.edu/publications/factsheets/energy/wind-energy-factsheet, Accessed on: 2024-03-30.

[18] A. Abu-Siada and S. M. Islam, "Applications of power electronics in renewable energy systems," in *Power Electronics Handbook*, 4th ed., 2023, pp. 797–843. [Online]. Available: https://www.sciencedirect.com/science/article/pii/B9780128114070000271, Accessed on: 2024-03-02.

[19] M. R. Sarkar, S. Julai, C. W. Tong, M. Uddin, M. F. Romlie, and G. M. Shafiullah, "Hybrid pitch angle controller approaches for stable wind turbine power under variablewind speed," *Energies*, vol. 13, 2020. [Online]. Available: https://doi.org/10.3390/en13143622, Accessed on: 2024-04-01.

[20] N. N. Sørensen and J. Johansen, "Aerodynamic investigation of winglets on wind turbine blades using CFD," Risø National Labratory, Roskilde, Denmark, 2006. [Online]. Available: https://orbit.dtu.dk/files/7703268/ris_r_1543.pdf, Accessed on: 2024-04-01.

[21] M. A. C. Queirolo, *Impact of Morphing Winglets on Aircraft Performance*, Msc thesis, Delft University of Technology, 2018. [Online]. Available: http://repository.tudelft.nl/., Accessed on: 2024-03-02.

[22] G. Giraldo, *CFD Modeling, Analysis, and Online Simulation For Beginners*, Simscale, 2023. [Online]. Available: https://www.simscale.com/blog/cfd-analysis-for-beginners/, Accessed on: 2024-04-10.

[23] M. Zawawi, A. Saleha et al, "A review: Fundamentals of computational fluid dynamics (CFD)," in *AIP Conference Proceedings*, vol. 2030, 2018. DOI: 10.1063/1.5066893.

[24] S. Team, *3 Core Components of CFD Analysis*, Spatial Corp, 2020. [Online]. Available: https://blog.spatial.com/cfd-analysis, Accessed on: 2024-04-16.

[25] Y. Abu-Zidan, P. Mendis, and T. Gunawardena, *Optimising the computational domain size in CFD simulations of tall buildings*, Department of Infrastructure Engineering, The Univeristy of Melbourne, 2021. DOI: 10.1016/j.heliyon.2021.e06723.

[26] Simscale, *What is a mesh*, 2023. [Online]. Available: https://www.simscale.com/docs/simwiki/preprocessing/what-is-a-mesh/, Accessed on: 2024-05-07.

[27] F. M. White, *Viscous Fluid Flow*, 3rd ed. McGraw-Hill Higher Education, 2006, ISBN: 0070697124.

[28] CFD Online, *Reynolds stress model*, 2017. [Online]. Available: https://www.cfd-online.com/Wiki/Reynolds_stress_model_(RSM), Accessed on: 2024-04-30.

[29] CFD Online, *Finite volume*, 2012. [Online]. Available: https://www.cfd-online.com/Wiki/Finite_volume, Accessed on: 2024-04-14.

[30] A. Farhan, A. Hassanpour, A. Burns, and Y. G. Motlagh, "Numerical study of effect of winglet planform and airfoil on a horizontal axis wind turbine performance," in *Renewable Energy*, vol. 131, 2019, pp. 1255–1273. DOI: 10.1016/j.renene.2018.08.017.

[31] M. G. Khalafallah, A. M. Ahmed, and M. K. Emam, "The effect of using winglets to enhance the performance of swept blades of a horizontal axis wind turbine," *Advances in Mechanical Engineering*, vol. 11, A. A. Gawad, Ed., 2019. DOI: 10.1177/1687814019878312.

[32] L. F. Monteiro, *Wind turbine*, Link to the orginal model for the wind turbine. Last updated 31-12-2018, 2015. [Online]. Available: https://grabcad.com/library/wind-turbine-72.

[33] Siemens Community, *Best Practices for Sliding Interfaces to accurately simulate Rigid Body Motion of fans/propellers*, 2024. [Online]. Available: https://community.sw.siemens.com/s/article/Best-Practices-for-Sliding-Interfaces-to-accurately-simulate-Rigid-Body-Motion-of-fans-propellers, Accessed on: 2024-05-06.

[34] S. Sicklinger, C. Lerch, R. Wüchner, and K. U. Bletzinger, "Fully coupled co-simulation of a wind turbine emergency brake maneuver," in *Journal of Wind Engineering and Industrial Aerodynamics*, vol. 144, 2015, pp. 134–145. DOI: 10.1016/j.jweia.2015.03.021.

[35] Siemens Community, *A new user's guide to Simcenter STAR-CCM+ simulation (Part 3/5): Meshing*, 2021. [Online]. Available: https://community.sw.siemens.com/s/article/A-new-user-s-guide-to-STAR-CCM-simulation-Part-3-5-Meshing, Accessed on: 2024-05-08.

[36] Applied Computational Fluid Dynamics, *Tutorial: Generation of a high-quality mesh for CFD simulations of wind turbines (STAR-CCM+)*, Youtube, Sep. 12 2022. [Online]. Available: https://www.youtube.com/watch?v=kaCoBw8ynhM.

[37] A. S. A. I. H. N. A., *The physical modelling and aerodynamics of turbulent flows around horizontal axis wind turbines*, 2017.

[38] M. M. Amiri, M. Shadman and S. F. Estefen, *URANS simulations of a horizontal axis wind turbine under stall condition using Reynolds stress turbulence models*, 2020.

A

Appendix 1

A.1 Specification of the mesh

Create Automated Mesh Operation			
Enable Meshers:			
	Surface Remesher	☑	
	Automatic Surface Repair	☑	
	Trimmed Cell Mesher	☑	
	Prism Layer Mesher	☑	
VRP			
-> Mesher -> Surface Remesher			
	Meshing Method	Triangle	
	Minimum Face Quality	0.2	
-> Mesher -> Automatic Surface Repair			
	Minimum Face Quality	0.2	
-> Mesher -> Trimmed Cell Mesher			
	Preform Mesh Alignment	☑	
-> Mesher -> Prism Layer Mesher			
	Stretching Function	Geometric Progression	
	Distribution Mode	Wall Thickness	
	Gap Fill Percentage	25	
	Minimum Thickness Percentage	0.01	
	Layer Reduction Percentage	0.01	
->Default Controls			
	Base Size	6 [m]	
	Target Surface Size	0.50%	
	Minimum Surface Size	0.50%	
	Number of Prisim Layers	13	
	Prisim Layer Near Wall Thickness	0.0000821595 [m]	
	Prisim Layer Total Thickness	0.043818234 [m]	
	->Volume Growth Rate		
		Default Growth Rate	very slow
		Surface Growth Rate	very slow
	Maximum Cell Size	8%	
-> Custom Controls -> Surface Control			
	Parts	Blades	
	-> Controls		
		Target Suface Size	custom

		Minimum Surface Size	custom	
	-> Values			
		Target Suface Size	0.50%	
		Minimum Surface Size	0.50%	
-> Custom Controls -> Surface Control 2				
	Parts	VRP		
	-> Controls			
		Target Suface Size	Custom	
		Minimum Surface Size	Custom	
		-> Prisim Layers		
			Prisim Layers	Custom
			Costumize Number of Layers	☑
			Costumize Total Thickness	☑
			Costumize Distribution	☑
	-> Values			
		Target Suface Size	8%	
		-> Custom Prisim Values -> Number of Prisim Layers	2	
		-> Custom Prisim Values -> Prisim Layer Near Wall Thickness	0.025	
		-> Custom Prisim Values -> Prisim Layer Total Thickness		
			Size Type	Absolut
			Absolut Size	0.05[m]
		Minimum Surface Size	8%	

VWT			
-> Mesher -> Surface Remesher			
	Meshing Method	Enhanced Quality Triangle	
	Minimum Face Quality	0.2	
-> Mesher -> Automatic Surface Repair			
	Minimum Face Quality	0.2	
-> Mesher -> Trimmed Cell Mesher			
	Preform Mesh Alignment	☑	
->Default Controls			
	Base Size	6 [m]	
	Target Surface Size	0.50%	
	Minimum Surface Size	0.50%	
	Prisim Layer Streaching	1.2	
	Prisim Layer Total Thickness	0.05 [m]	

	->Volume Growth Rate		
		Default Growth Rate	very slow
		Surface Growth Rate	very slow
	Maximum Cell Size	256%	
-> Custom Controls -> Surface Control			
	Parts	VRP	
	-> Controls		
		Target Suface Size	custom
		Minimum Surface Size	custom
	-> Values		
		Target Suface Size	8.00%
		Minimum Surface Size	8.00%
-> Custom Controls -> Surface Control 2			
	Parts	Bottom, Top, Side, Side 2, Inlet, Outlet	
	-> Controls		
		Target Suface Size	Custom
		Minimum Surface Size	Custom
		Prisim Layers	Disable
	-> Values		
		Target Suface Size	256%
		Minimum Surface Size	256%
-> Custom Controls -> Volumetric Control			
	Parts	Wake Refinement Cylinder	
	-> Controls -> Trimmer		
		Custom Isotropic Size	☑
	-> Values		
		Custom Size	16%

A.2 Prism layers parameters

Calculated prism layer parameters, 10 m/s					
Skala	**1**			**0,6**	
bas tjocklek	3,94	m		2,364	m
Radie	47,62	m		28,572	m
Topp tjocklek	1,8	m		1,08	m
Radie bas	8	m		4,8	m
Physic properites					
y +	200			200	
μ	0,0000185508	Pa*s			
Air density	1,18415	kg/m^3			
ν	0,00001566592	m2/s		0,00001566592	
U topp	60,8276253	m/s		101,3793755	m/s
U bas	14,19867374	m/s		23,66445623	m/s
Wind Speed	**10**	m/s		16,66666667	m/s
Re bas	3570985,426			3570985,426	
Re topp	6989038,667			6989038,667	
TSR (Tip Speed Ratio)	6			6	
Wing tip speed	60	m/s		100	m/s
Wing base speed	10,0797984	m/s			
Wing rotation rate	0,2005312177	rps		0,5570311602	rps
Prism layer parameters					
boundary thickness	0,07303039035	m		0,04381823421	m
FLT (First layer thickness)	0,00136932505	m		0,00082159503	m
r (stretching factor)	1,2			1,2	
m (Number of layers)	13,47472191			13,47472191	

Calculated prism layer parameters, 7.5 m/s					
Skala	**1**			**0,6**	
bas tjocklek	3,94	m		2,364	m
Radie	47,62	m		28,572	m
Topp tjocklek	1,8	m		1,08	m
Radie bas	8	m		4,8	m
Physic properites					
y +	200			200	
μ	0,0000185508	Pa*s			
Air density	1,18415	kg/m^3			
ν	0,00001566592	m2/s		0,00001566592	
U topp	45,62071898	m/s		76,03453163	m/s
U bas	10,6490053	m/s		17,74834217	m/s
Wind Speed	**7,5**	m/s		12,5	m/s
Re bas	2678239,07			2678239,07	
Re topp	5241779			5241779	
TSR (Tip Speed Ratio)	6			6	
Wing tip speed	45	m/s		75	m/s
Wing base speed	7,559848803	m/s			
Wing rotation rate	0,1503984133	rps		0,4177733701	rps
Prism layer parameters					
boundary thickness	0,07609428013	m		0,04565656808	m
FLT (First layer thickness)	0,00178519649	m		0,00107111789	m
r (stretching factor)	1,2			1,2	
m (Number of layers)	12,3623517			12,3623517	

Calculated prism layer parameters, 5 m/s					
Skala	**1**			**0,6**	
bas tjocklek	3,94	m		2,364	m
Radie	47,62	m		28,572	m
Topp tjocklek	1,8	m		1,08	m
Radie bas	8	m		4,8	m
Physic properites					
y +	200			200	
μ	0,0000185508	Pa*s			
Air density	1,18415	kg/m^3			
ν	0,00001566592	m2/s		0,00001566592	
U topp	30,41381265	m/s		50,68968775	m/s
U bas	7,099336868	m/s		11,83222811	m/s
Wind Speed	**5**	m/s		8,333333333	m/s
Re bas	1785492,713			1785492,713	
Re topp	3494519,334			3494519,334	
TSR (Tip Speed Ratio)	6			6	
Wing tip speed	30	m/s		50	m/s
Wing base speed	5,039899202	m/s			
Wing rotation rate	0,1002656088	rps		0,2785155801	rps
Prism layer parameters					
boundary thickness	0,08063208816	m		0,0483792529	m
FLT (First layer thickness)	0,00259202392	m		0,00155521435	m
r (stretching factor)	1,2			1,2	
m (Number of layers)	10,84386424			10,84386424	

A.3 Physics parameters

☑	Cell Quality Remedition					
☑	All y+ Wall Treatment					
☑	Wall Distance					
☑	Eliptic Blending					
☑	Reynolds Stress Turbolence					
☑	Reynolds-Average Navier-Stokes					
☑	Turbulent					
☑	Constant Density					
☑	Gradients					
☑	Segregated Flow					
☑	Gas					
☑	Implicid Unsteady					
☑	Three Dimensional					

Velocity	[16.66666667, 0, 0]	[m/s]	
Motions -> Rotation			
	Axis Direction	[-1, 0, 0]	
	Rotating rate	33.42186961	[RPM]

Regions -> VRP			
	Rotating Part -> Physics Conditions		
		Shear Stress Specification	Slip
	Physics values -> Motion Specification		
		Motion	Rotation

Regions -> VWT						
	Boundaries					
		Inlet				
			Type	Velocity Inlet		
			Phsics Values			
				Velocity Magnitude	16.66666667	[m/s]
				Turbulens Intensity		
					Value	0.01
		Outlet				
			Type	Pressure Outlet		
		Top, Bottom, Side 1, Side 2, RotatingPart				
			Phsics Conditions			
				Shear Stress Specification	Slip	

DEPARTMENT OF MECHANICS AND MARITIME SCIENCES
CHALMERS UNIVERISTY OF TECHNOLOGY
Gothenburg, Sweden 2024
www.chalmers.se

CHALMERS